

Extreme value analysis of ground magnetometer observations at Valentia Observatory, Ireland

Alexandra Ruth Fogg¹, Caitriona M Jackman², John Malone-Leigh¹, Peter Gallagher³, Andrew W Smith⁴, Mark Lester⁵, Maria-Theresia Walach⁶, and James Edwin Waters⁷

¹School of Cosmic Physics, DIAS Dunsink Observatory, Dublin Institute For Advanced Studies

²Dublin Institute for Advanced Studies

³DIAS

⁴Northumbria University

⁵University of Leicester

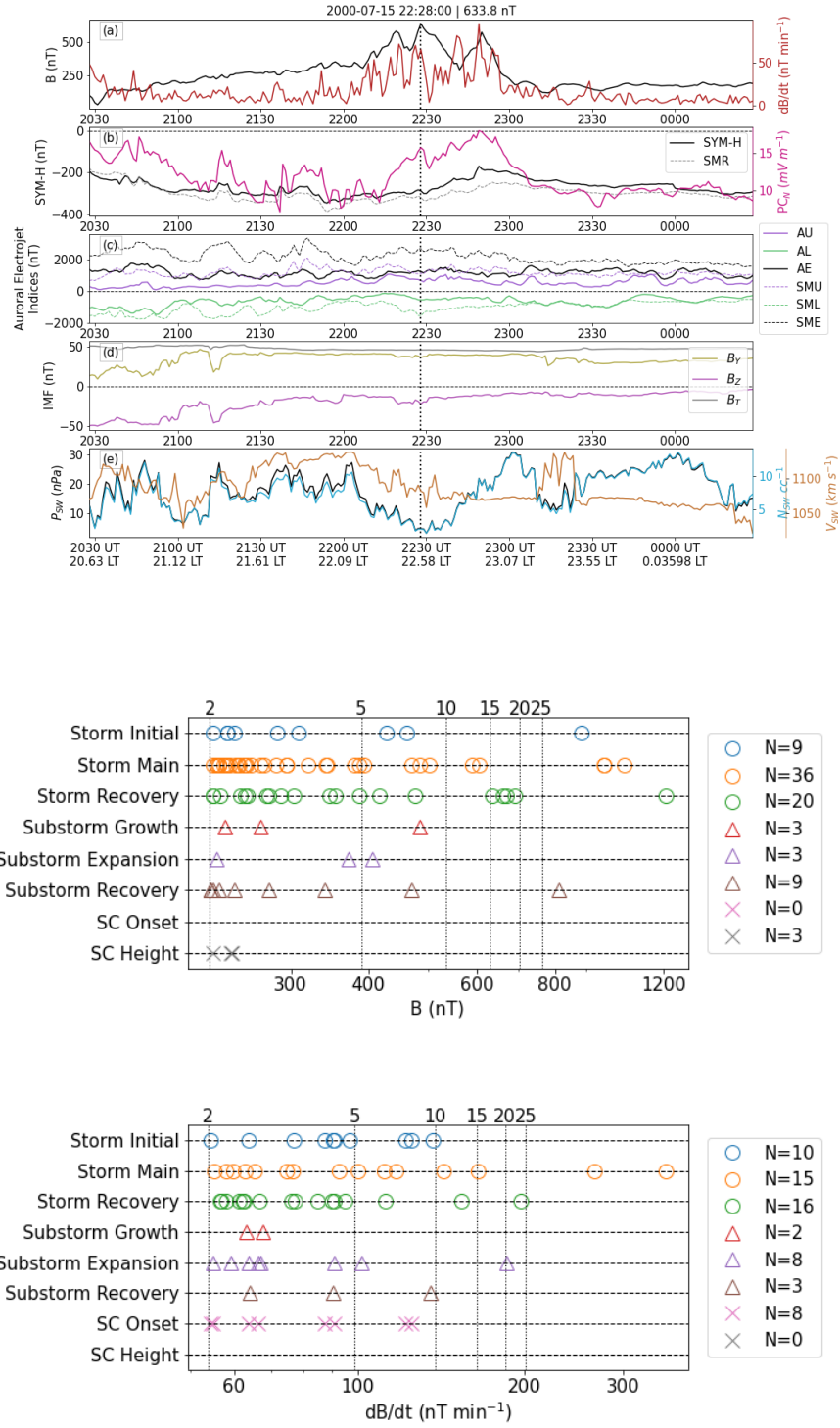
⁶Lancaster University

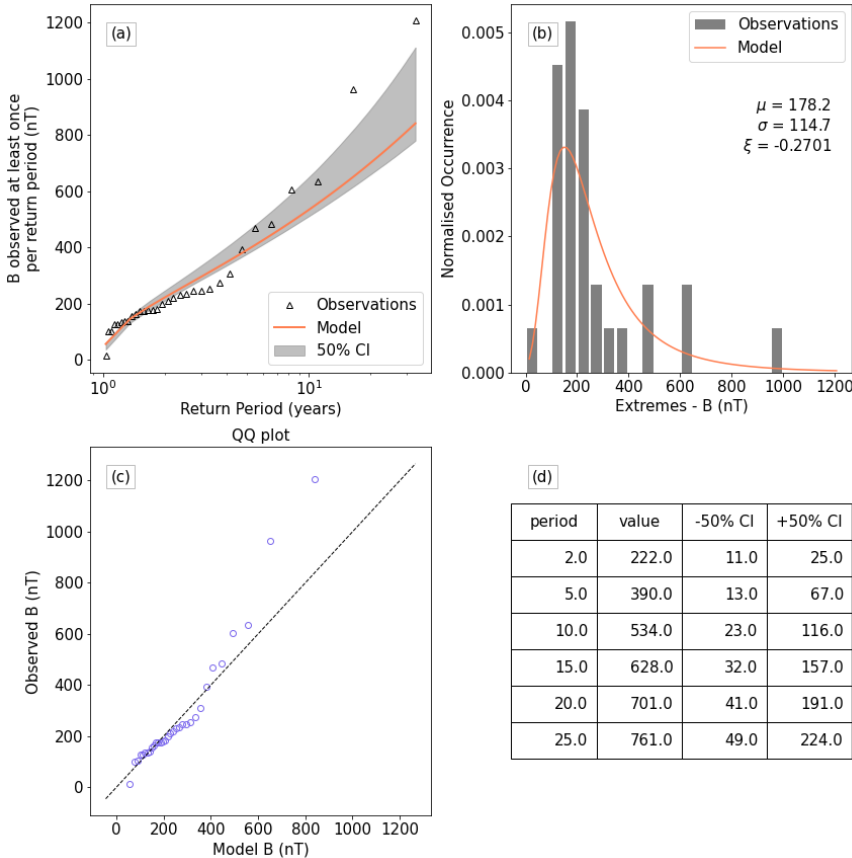
⁷Laboratoire d'Astrophysique de Marseille

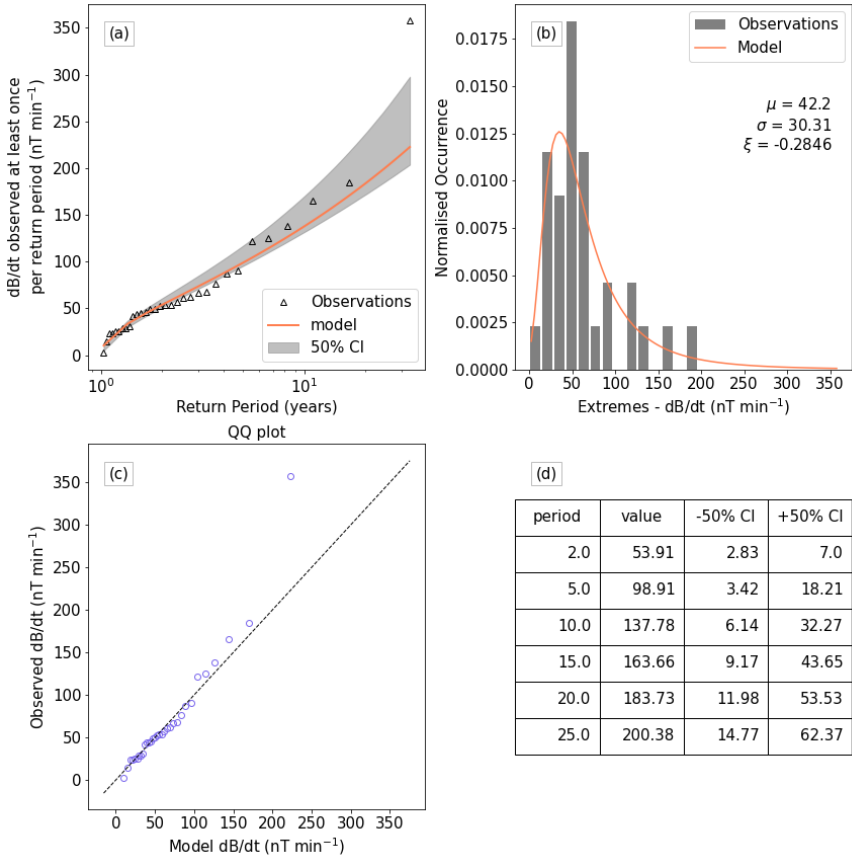
May 25, 2023

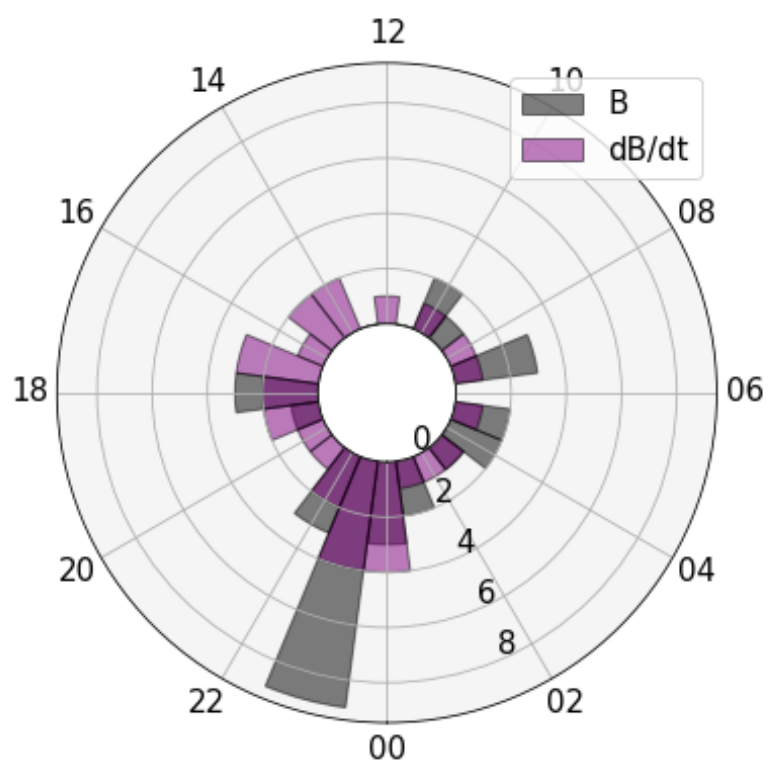
Abstract

Understanding global space weather effects is of great importance to the international scientific community, but more localised space weather predictions are important on a national level. In this study, data from a ground magnetometer at Valentia Observatory is used to characterise space weather effects on the island of Ireland. The horizontal component of magnetometer observations and its time derivative are considered, and extreme values of these are identified. These extremes are fit to a generalised extreme value distribution, and from this model return values (the expected magnitude of an observation within a given time window) are predicted. The causes of extreme values are investigated both in a case study, and also statistically by looking at contributions from geomagnetic storms, substorms, and sudden commencements. This work characterises the extreme part of the distribution of space weather effects on Ireland (and at similar latitudes), and hence examines those space weather observations which are likely to have the greatest impact on susceptible technologies.









Extreme value analysis of ground magnetometer observations at Valentia Observatory, Ireland

Alexandra Ruth Fogg¹

C. M. Jackman¹, J. Malone-Leigh¹, P. T. Gallagher¹, A. W. Smith², M. Lester³, M. -T. Walach⁴, J. E. Waters⁵

¹School of Cosmic Physics, DIAS Dunsink Observatory, Dublin Institute for Advanced Studies, Dublin 15, Ireland

²Department of Mathematics, Physics and Electrical Engineering, Northumbria University, Newcastle upon Tyne, UK

³School of Physics and Astronomy, University of Leicester, UK

⁴Lancaster University, Physics Department, Bailrigg, LA1 4YW, UK

⁵Aix Marseille Univ, CNRS, CNES, LAM, Marseille, France

Key Points:

- Extreme observations at Valentia MagIE station are identified; more are observed in the premidnight sector
- Return values of extreme Valentia observations at given return periods are predicted
- Implications of space weather phenomena on extreme observations at Irish latitudes are examined

Abstract

Understanding global space weather effects is of great importance to the international scientific community, but more localised space weather predictions are important on a national level. In this study, data from a ground magnetometer at Valentia Observatory is used to characterise space weather effects on the island of Ireland. The horizontal component of magnetometer observations and its time derivative are considered, and extreme values of these are identified. These extremes are fit to a generalised extreme value distribution, and from this model return values (the expected magnitude of an observation within a given time window) are predicted. The causes of extreme values are investigated both in a case study, and also statistically by looking at contributions from geomagnetic storms, substorms, and sudden commencements. This work characterises the extreme part of the distribution of space weather effects on Ireland (and at similar latitudes), and hence examines those space weather observations which are likely to have the greatest impact on susceptible technologies.

Plain Language Summary

Space weather describes the effects of the interaction between the Sun's solar wind and the Earth's magnetic field, and can have dramatic impacts on human technology. Space weather can be characterised both globally, and on a local level. In this study, space weather over the island of Ireland is characterised using an Irish ground based magnetometer at Valentia Observatory. Extreme observations from this magnetometer are detected, and these are used to predict future extreme observations. Additionally, the contributions of different types of space weather phenomena to extreme observations are determined. Understanding extreme observations on a national level will help to enhance space weather resilience which is increasingly important as society becomes more and more dependent on technology.

1 Introduction

Ground based magnetometers measure deflections in the magnetic field as a result of changes in overhead currents, which can be used to infer variations in geomagnetically induced currents (GICs, Blake et al., 2016, 2018), geoelectric fields (Campanyà et al., 2019; Malone-Leigh et al., 2023), and the overhead currents themselves (e.g. auroral electrojet indices, Davis & Sugiura, 1966). Ground based magnetometers have been used for over a century to characterise space weather effects. As the amount of data recorded at stations builds up over time, a wealth of information can be unravelled from these expanding datasets using new and/or more computationally intensive data analysis techniques.

Space weather impacts a breadth of human technology, and some technology is more susceptible than others. For example, recently 38 starlink satellites were lost to a minor-moderate size geomagnetic storm (Fang et al., 2022), while infrastructure like power grids are more robust to all but the most extreme events (Bolduc, 2002). As we move to an increasingly technologically-reliant society, these space weather risks become of greater importance, and indeed space weather is listed on national risk registers in, for example, the United Kingdom. Therefore the motivation for understanding, and indeed predicting the most extreme space weather events is of the utmost importance.

In this study, observations from an Irish magnetometer station will be characterised using Extreme Value Analysis (EVA). By using this technique, extreme observations will be identified, and after fitting a model, return values of these extreme observations will be extracted. These return values describe the value that will be observed at least once in a given return period. Characterisation of return values enables understanding of what

is (or indeed, isn't) an extreme observation, and how regularly these might occur. Understanding this is a fundamental part of interpreting space weather at Irish latitudes, and in relation to specific Irish geology.

Although it's an emerging technique in space science, EVA is used more commonly in other fields to predict the return periods of e.g., earthquakes or extreme weather (e.g., Finkel et al., 2023). EVA has also been used by some authors to predict the return period or probability of extreme Space Weather events. A limitation of the technique is the fitting of a model to detected extremes: a large amount of data is needed to result in a large number of extremes for the fitting. For example, Siscoe (1976) extracted the three largest events from each solar cycle in 91 years of aa index, and calculated statistical characteristics for the extreme values. Subsequently, Silbergleit (1996) identified sudden storm commencements between 1957 and 1980, and by fitting a Gumbel distribution predicted that a $|Dst|$ value above 400 nT would be observed within the 17 (± 3) years that followed 1980. Similarly, Silbergleit (1999) utilised the aa index between 1868 and 1992 (124 years), separating between odd and even solar cycles to account for Hale cycle affects. They predicted that a geomagnetic event equalling the March 1989 event (e.g., Bolduc, 2002) would occur within the next 8 odd or 13 even solar cycles.

Koons (2001) determined return values using 66 years of geomagnetic index Ap, as well as proton and electron fluxes. Additionally, Tsubouchi and Omura (2007) identified geomagnetic storms from 44 years of Dst data, and calculated that the return period of an event such as the March 1989 storm is approximately 60 years. Riley and Love (2017) also detected storms in the Dst index, and by fitting a power law estimated the probability of extreme events in Dst. Recently, Elvidge (2020) used EVA on aa index data, which spans 150 years; they first removed a strong solar cycle variation from the data using a Hilbert-Huang transform, and then predicted return values with periods up to 1000 years, separating data into solar cycle minimum and maximum. Bergin et al. (2023) performed EVA on Dst, SYM-H and SMR and compared the differences between the return values of these similar indices. These analyses can provide answers towards understanding one of the key questions in the field of space weather: when will the next dramatic space weather event be?

Similarly to this study, Thomson et al. (2011) estimated return values at magnetometer stations across Europe, including Irish station Valentia (51.93°N , 349.75°E geographic, with data from 1995-2010). Despite only using 15 years of data to fit the model, they estimated 100 and 200 year return values of both the horizontal component of the magnetic field and its time derivative. From their Figures 5 and 6, they predict a 100 year return value of 2000 nT for H and 1000 nT minute^{-1} for $\frac{dH}{dt}$. Rogers et al. (2020) takes a similar approach, and examines trends with latitude and magnetic local time. Uniquely in this study, a larger amount of data will be used, and the model will not be extrapolated beyond the bounds of the length of the data. Additionally, unlike these previous papers, an in depth analysis of one station will be presented, including specific return values, and an investigation of the causes of extreme values.

Finally, the causes of high values at an Irish magnetometer station will be investigated by considering the contributions of storms, substorms and sudden commencements (SCs). Geomagnetic storms are generated when solar wind - magnetosphere coupling is strong and prolonged; this results in enhancements in geomagnetic activity, and ultimately the storm itself. Geomagnetic storms are characterised by three phases (e.g., McPherron, 1995; Hutchinson, Wright, & Milan, 2011; Walach & Grocott, 2019): initial, main, and recovery. During the main phase, a large amount of energy is deposited in the ring current, leading to a characteristic decrease in the ring current index, SYM-H.

Following the onset of magnetic reconnection at the dayside, open magnetic flux is pulled across the polar cap and builds up in the magnetotail. As a result, the mag-

netotail flares and presents a larger surface area to the solar wind, increasing the pressure within the magnetotail. This increased pressure cannot be maintained and magnetic reconnection begins in the magnetotail, resulting in a large deposition of energy into the nightside ionosphere, and effects are seen across a range of phenomena including ionospheric convection (e.g., Bristow et al., 2001, 2003; Bristow & Jensen, 2007), field-aligned currents (FACS, e.g., Sangha et al., 2020), aurorae (e.g., Nishimura et al., 2020), auroral kilometric radiation (e.g., Waters et al., 2022), and increased magnetic activity (Freeman et al., 2019). First characterised by McPherron (1970), substorms are generally divided into three phases: growth, expansion and recovery, and exhibit intense variability of the phenomena listed above.

Sudden commencements (SCs, Araki, 1994) are swift compressions of the Earth’s magnetosphere driven by rapid increases in solar wind dynamic pressure known as pressure pulses. A characteristic step change signature is seen in the ring current index SYM-H (e.g., Araki, 1994; Gillies et al., 2012; Hori et al., 2015) as a result of an increase in the geomagnetic field in the equatorial plane. In this paper, SCs are divided into two phases: ‘onset’ defines from the start of the step change in SYM-H (as detected by an event list described later) to the end of the step change. The ‘height’ phase is then the period 10 minutes after the end of the step change. SCs effects span the magnetosphere-ionosphere system, and can include ULF waves (e.g., Oliveira et al., 2020) and enhancements in ionospheric convection / aurorae / FACs (e.g., Fogg et al., 2023). SCs can be further divided into events rapidly followed by a geomagnetic storm, known as sudden storm commencements (SSCs), and those not followed by a storm, known as sudden impulses (SIs). For the purpose of this study, only the duration of the SC increase and the 10 minutes that follow will be considered. Although some differences are seen between SSCs and SIs by (e.g., Smith et al., 2019, 2021), this will not affect answering the question of whether SCs can drive extreme events in magnetometer observations.

2 Data

2.1 Magnetometer Data

The Magnetometer Network of Ireland (MagIE, <https://www.magie.ie/>), includes stations across the island of Ireland, and has been used to model the effects of geomagnetically induced currents (Blake et al., 2016, 2018) and geoelectric fields (Campanyà et al., 2019; Malone-Leigh et al., 2023). Most recently, Malone-Leigh et al. (2023) used the MagIE network to nowcast geoelectric fields. Of course, MagIE is one of many magnetometer networks across the world, and the Valentia station in the southwest of Ireland (51.93°N, 349.75°E geographic) is a contributing station to the INTERMAGNET network, which itself contributes to the SuperMAG dataset (Gjerlov, 2012). In this study, data from the MagIE Valentia station is used, as it provides a broad parameter space of two solar cycles; data from 1991-2021 is extracted via the SuperMAG interface at one minute resolution.

Key to this study is the horizontal component of the magnetic field, B , which is calculated using Equation 1:

$$B = \sqrt{N^2 + E^2} \quad (1)$$

from the magnetic north (N) and magnetic east (E) components of the magnetic field observations. The rate of change of the horizontal component, $\frac{dB}{dt}$, is also calculated similarly to Smith et al. (2019) using Equation 2:

$$\frac{dB}{dt} = \frac{\sqrt{[N(t+dt) - N(t)]^2 + [E(t+dt) - E(t)]^2}}{dt} \quad (2)$$

where N and E are as defined previously, and dt is the time elapsed between measurements at t and $t + dt$. Both B and $\frac{dB}{dt}$ are calculated at 1 minute resolution.

2.2 Event lists

In order to compare predicted return values with geomagnetic phenomena, event lists of these phenomena are utilised, which will be described here. The geomagnetic storm list compiled by Walach and Grocott (2019) is used in this manuscript to compare storm time values to the predicted return values. Storms are detected in a manner similar to that of Hutchinson, Wright, Milan, Grocott, and Boakes (2011), by searching for a characteristic shape in SYM-H observations. In this manuscript, 314 geomagnetic storms from this list are utilised from 1991-2019 inclusive, as this overlaps with Valentia data availability described above. The effects of geomagnetic storms captured by this list has been studied extensively (e.g., Wharton et al., 2020; Sandhu et al., 2021; Orr et al., 2023).

In this manuscript the Substorm Onsets and Phases From Indices of the Electrojet (SOPHIE, Forsyth et al., 2015) substorm list is used to identify substorm phases in Valentia data. The SOPHIE detection algorithm identifies characteristic substorm signatures in SML, the SuperMAG equivalent of the lower envelope of the auroral electrojet index. Two additional processing steps are applied to the SOPHIE event list to produce a list of individual substorms with three phase start times, in a similar sense to Waters et al. (2022). Firstly, any expansion phase onsets which may be attributed to steady magnetospheric convection are removed; this is flagged directly in the event list. Secondly, individual substorms with growth directly followed by expansion and recovery phase are extracted; all other identified phases are removed. This results in over 26,000 substorms being extracted from the 75% EPT (Expansion Percentile Threshold) list, covering 1996-2014. Similarly to the Walach and Grocott (2019) storm list, the SOPHIE list has been used extensively to study the effects of substorms on the terrestrial magnetosphere (e.g., Waters et al., 2022).

Additionally, a list of SCs is compiled by the Observatori de l'Ebre (hereafter OE events, Observatori de l'Ebre, 2020). In this study, 432 positive SCs between 1995 and 2020 inclusive are extracted from the OE event list, and used to characterise to what extent SCs contribute to extreme observations. This window gives a broad parameter space of two solar cycles. The OE event detection algorithm searches for rapid variations in the traces of magnetometer stations at roughly equatorial latitude ($\approx 33^\circ N$). Any increase with a gradient of at least 3 nT min^{-1} is recorded as an SC. This event list was commissioned by the International Association of Geomagnetism and Aeronomy (IAGA), and is part of its International Service of Geomagnetic Indices (ISGI), and has been used by authors to characterise the propagation of SC effects through the magnetosphere (e.g., Gillies et al., 2012; Fogg, 2021; Fogg et al., 2023).

2.3 IMF, solar wind and geomagnetic indices

Finally, upstream observations and geomagnetic indices are extracted from the OMNI (Weimer et al., 2002, 2003; Weimer & King, 2008; King & Papitashvili, 2005) dataset to analyse the causes of an example extreme observation in B . All these data are retrieved from OMNIWeb (<https://omniweb.gsfc.nasa.gov/hw.html>) at 1 minute resolution. The B_Z and B_Y components are used to characterise the interplanetary magnetic field (IMF), along with the solar wind dynamic pressure (P_{SW}), proton density (N_{SW}) and solar wind velocity (V_{SW}). Additionally, geomagnetic indices SYM-H, PC_N , AE, AU and AL are retrieved from OMNIWeb. The ring current index SYM-H is provided by the World Data Center for Geomagnetism Kyoto (Iyemori, 1990) and is derived from near equatorial latitude magnetometer stations; SYM-H shows signatures characteristic of geomagnetic storms. Analogous to SYM-H, SuperMAG index SMR (Newell & Gjerloev, 2012) is derived from all available magnetometer stations between -50° and $+50^\circ$ geomagnetic

latitude. Similarly, the auroral electrojet indices (AE, AU and AL, World Data Center for Geomagnetism Kyoto et al., 2015; Davis & Sugiura, 1966) are derived from auroral latitude magnetometer observations and demonstrate activity in the auroral zone; AL shows characteristic substorm signatures. SuperMAG equivalents SME, SMU and SML (Newell & Gjerloev, 2011) are also used in this manuscript, which are derived from all available magnetometer stations between 40° and 80° geomagnetic latitude. Finally, the polar cap index PC_N (provided by the World Data Center for Geomagnetism, Copenhagen, Troshichev et al., 1979; Troshichev & Andrezen, 1985; Stauning, 2013) is derived from the variation in the trace of a polar latitude magnetometer and information from the solar wind and IMF variability; PC_N is an indicator of the speed of flux transport across the polar cap.

3 Extreme Value Analysis

In this manuscript, *Extreme Value Theory* is used to both extract extreme events from Valentia observations, and then use these events, fitting to a model, to estimate the return values of Valentia observations. This analysis will be called extreme value analysis or ‘EVA’ in the text, and will allow quantification of the baseline conditions at Valentia. This allows understanding of what is, or indeed isn’t, an unusually elevated value at the station, and indeed at similar stations at this latitude. In turn, this will enhance interpretation of magnetometer observations at this latitude, allowing characterisation of whether an event is unusual. Indeed, this work will describe the likelihood of extreme events within a given time frame, and characterise the rarity of previous events at Irish latitudes.

To conduct the EVA, the python package `pyextremes` is used, along with the package `emcee` (Foreman-Mackey et al., 2013) for Markov Chain Monte Carlo (MCMC) fitting. `pyextremes` is used to extract the extremes, fit them to a model (described below) using `emcee` (used previously by Smith et al., 2018), and use the fitted model to predict return values. Unlike in Elvidge (2020), in this paper the Valentia B and $\frac{dB}{dt}$ data are not corrected for solar cycle variations before the EVA is performed. When B and $\frac{dB}{dt}$ were plotted along with sunspot number, no significant variation with solar cycle was observed. Therefore it was deemed that the EVA could be performed on the data directly, without removing solar cycle variations. It is important to note that because the data spans a broad parameter space of two solar cycles, the results may be applicable to both past and future events.

3.1 Detecting Extremes

The first stage of the EVA is to detect extremes from the dataset. In this manuscript extremes are detected using the block maxima method (as opposed to peaks over threshold, to avoid user bias in choosing a threshold). Similarly to Elvidge (2020), the data are divided into calendar years, and the highest observation within that calendar year is detected as an extreme value; note that full calendar years of Valentia data are used from 1991-2021, including years with any operational data gaps. The effect of the chosen block size (i.e. calendar year in this case) on the distribution of the detected extremes was tested. For three different block sizes (calendar year, 180 days, and 90 days) the distribution of the detected extremes was plotted. The distributions were very similar across all block sizes, even though more extremes are detected for shorter block sizes. Since the distribution of extremes was the same across different block sizes, a calendar year was chosen as the block size for this study as it will capture the full cycle of ionospheric seasonality, and therefore a broad parameter space of observations. Extremes are detected in this manner for both B, and $\frac{dB}{dt}$.

Firstly, an example of an extreme in Valentia B observations will be presented. In Figure 1, the third highest B extreme (the highest with continuous IMF and plasma data)

is presented across a variety of geomagnetic indices and IMF and plasma data. In panel 1(a), Valentia B and $\frac{dB}{dt}$ observations are presented in black and red respectively. B comes to a peak of 634 nT at 22:28 UT on 15th July 2000, with smaller peaks shortly before and after. Interestingly, $\frac{dB}{dt}$ comes to a local peak about twenty minutes later, although the detected extreme for that year occurs at 14:48 UT on the same day. Indeed, in 43.75% (14 in 31) of calendar years investigated, the detected B and $\frac{dB}{dt}$ extreme occur within 1 day of each other. This suggests that these extremes may be driven by some shared driver, perhaps a geomagnetic storm.

Presented in panel 1(b), the ring current index SYM-H is well below the quiet level of -15 nT described by Walach and Grocott (2019), and reaches below -200 nT at the time of the peak; this likely indicates an ongoing geomagnetic storm. SMR is similar to SYM-H in this interval. PC_N is highly elevated above the average values of 0.79 mV m⁻¹ (Fogg et al., 2022), reaching beyond 15 mV m⁻¹. This indicates strong polar electro-dynamics, and likely rapid transport of magnetic flux antisunwards across the polar cap. Although no obvious substorm signatures are present in AL (green curve in panel 1(c)), all of the auroral electrojet indices are highly elevated above average values (66 nT for AU, and -77 nT for AL (Fogg et al., 2022)), indicating strong activity in the auroral zone and potentially bright auroral emission. Given the strong driving in the interval, it is possible that the auroral oval has expanded beyond the range of magnetometers contributing to AE/AU/AL, so SuperMAG indices SME/SMU/SML are included as they cover a larger range in latitude. For all three indices comparisons (e.g. AE versus SME etc), the traditional auroral electrojet index is underestimating the value of the auroral electrojet as measured by SuperMAG indices (as characterised statistically by Bergin et al., 2020). However the interpretation in this interval is similar: strong driving in the auroral zone with no clear substorm signatures.

IMF B_Y (yellow) and B_Z (purple) are presented in panel 1(d), along with the total IMF magnitude ($B_T = \sqrt{B_X^2 + B_Y^2 + B_Z^2}$, grey). At the start of the interval, IMF B_Z is strongly southwards, with values reaching -50 nT, while B_Y has a slightly lower magnitude, but is strongly positive. Although the balance of B_Z and B_Y changes, and B_Y becomes dominant, there is strong negative B_Z throughout the interval. This suggests that there is strong solar wind - magnetosphere coupling at the subsolar point in the form of magnetic reconnection, resulting in a large amount of energy being communicated into the magnetosphere. Additionally, the solar wind dynamic pressure, which is presented in panel 1(e), varies greatly throughout the interval, sometimes exceeding 25 nPa (over 10 times the average of 1.83 nPa presented by Fogg et al. (2022)). The pressure curve is dominated by the shape of the proton density (blue in panel 1(e)), which sometimes exceeds 10 cc⁻¹, over double average values presented by Fogg et al. (2022). Finally, the solar wind velocity is also highly elevated, sometimes exceeding 1100 km s⁻¹, over double average values of 439 km s⁻¹ presented by Fogg et al. (2022).

Combining these observations, it is clear that in the lead up to the observed extreme, the magnetosphere is being strongly driven by negative B_Z , with a strong B_Y component (B_Y has also been shown to increase reconnection rates by altering the position of the reconnection site (e.g., Grocott et al., 2003, 2004, 2008)), and high solar wind dynamic pressure resulting in a compressed magnetosphere. This results in storm activity in the ring current index SYM-H (strongly negative) and enhanced activity in polar and auroral electro-dynamics, although this may not be directly driven by the solar wind. Additionally, it is important to note that the Valentia station is around 23 magnetic local time (MLT) at the time this extreme is observed; the MLT dependence of the observed extremes will be examined next.

A histogram of the extremes detected in both B and $\frac{dB}{dt}$ with respect to the MLT of the Valentia station at detection time is presented in Figure 2 (B extremes in grey, $\frac{dB}{dt}$ extremes in purple). For both B and $\frac{dB}{dt}$, more extremes are detected in the pre-midnight sector than elsewhere, although the difference is particularly stark for B. This may

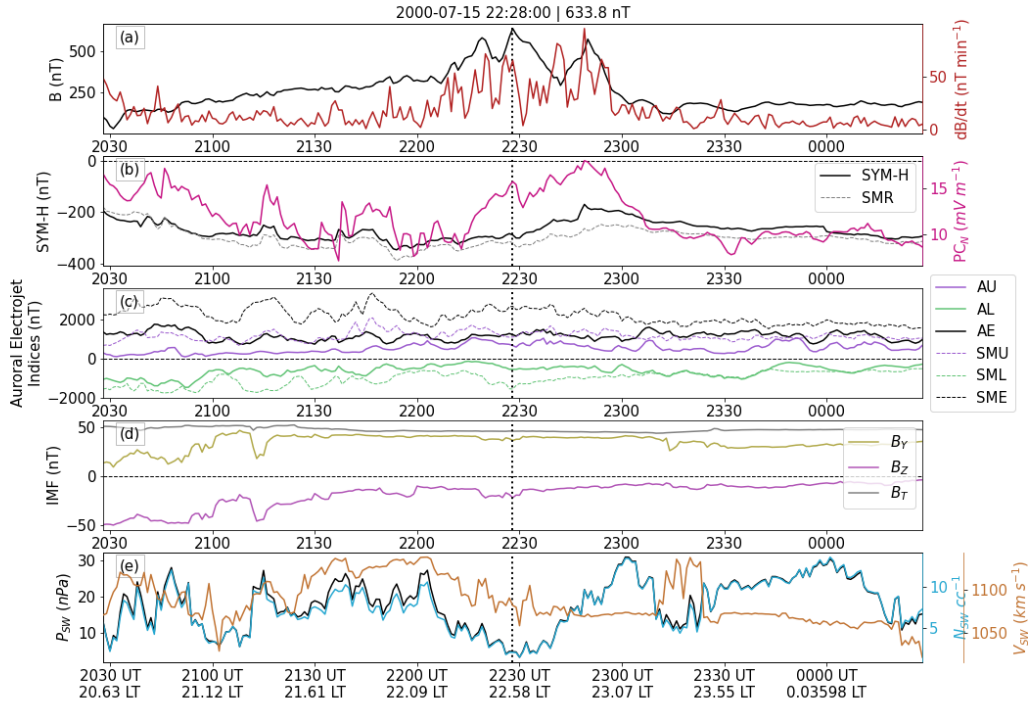


Figure 1. Timeseries of (a) Valentia B (black) and $\frac{dB}{dt}$ (red) (b) SYM-H (black), SMR (grey/dashed) and PC_N (pink) (c) auroral electrojet indices (solid) and SuperMAG equivalents (dashed) (d) IMF B_Y (yellow) and B_Z (purple) components, with total IMF magnitude $B_T = \sqrt{B_X^2 + B_Y^2 + B_Z^2}$ (grey) (e) solar wind pressure (black), proton density (blue) and solar wind velocity (gold). Centred on the detected B extreme at 22:28 UT on 15/07/2000, vertical dashed line indicates this time in all panels. The universal time is indicated on all axis ticks, and for panel (e) the magnetic local time of Valentia is also indicated.

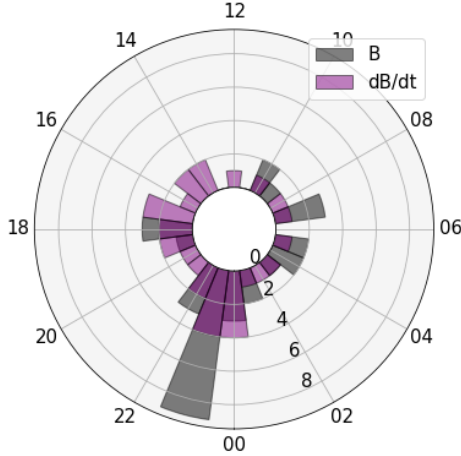


Figure 2. Histogram of the number of detected extremes with respect to the MLT of the Valentia magnetometer at the time of detection. Bins are 1 hr MLT in width, and are centred on each hour of MLT; radial length of the bar indicates the amount of extremes detected in that bin. Dark grey for extremes in B , purple for extremes in $\frac{dB}{dt}$.

relate to Valentia being in the region where substorm onset is most often occurs. However, $\frac{dB}{dt}$ changes may also be driven by step changes relating to compressional wave propagation through the magnetosphere, for example as a result of SCs (e.g., Araki, 1994; Hori et al., 2015; Fogg et al., 2023); this may be why more $\frac{dB}{dt}$ extremes are seen at day-side MLTs than for B .

3.2 Modelling the distribution of B extremes

Having extracted the extremes using the block maxima method described above, these are used to fit a *Generalised Extreme Value Distribution* (GEVD). The GEVD is defined in terms of:

$$G(x) = \exp \left(-1 \left[1 + \xi \left(\frac{x - \mu}{\sigma} \right) \right]^{-\frac{1}{\xi}} \right) \quad (3)$$

using the same notation as Elvidge (2020), where μ is the location parameter, σ is the scale parameter, and ξ is the shape parameter. The model is fitted using MCMC fitting as implemented in the `emcee` python package; for full details, the reader is directed to Foreman-Mackey et al. (2013).

In the limit where ξ goes to 0, the GEVD distribution becomes the Gumbel distribution:

$$G(x) = \exp \left(-\exp \left[-\frac{x - \mu}{\sigma} \right] \right) \quad (4)$$

with parameters defined as for equation 3. `pyextremes` automatically selects between the GEVD and Gumbel distributions depending on which fits the data better. Best

fit is characterised using the Akaike Information Criterion (AIC, Akaike, 1974): whichever distribution has the smaller AIC is chosen as it has a more optimal fit.

Figure 3 presents several ways of assessing the fit of the GEVD distribution for the B extremes. Firstly, in panel 3(a), the observed extremes are plotted as a function of their return period (triangles), with the modelled extremes overplotted as an orange curve, with 50% confidence interval as a grey shade. The model fits the data best where there are most observed extremes: at the lower end of the y axis. However, around 20-40 years return period, the fit of the model strays away from the data. At the high end of the extremes, the extremes do not fall within the confidence interval. Overall, this suggests that the model is better at predicting the lower extremes, i.e. those with lower return periods; this will be independent of block size, since the distribution of extremes is.

In panel 3(b), the probability distribution functions for the observed and modelled extremes are compared, with observations in grey and the model in orange. The model follows the general shape of the observed distribution, but does not reach the same peak as the observations, and over/under estimates in areas, particularly towards higher B. Note the location, scale and shape parameters are recorded on this panel for repeatability. Finally, the distributions of observed and modelled B are compared in a quantile-quantile (or QQ) plot, allowing examination of the relative shape of the distributions. For each observed extreme B, the modelled B of the same probability is extracted, and these two B values are plotted against each other. Where the values lie on the $y=x$ line, the distributions agree, otherwise, they differ. In some places, the points lie on or very close to the $y=x$ line, but as the distributions extend to higher B (where there are less observed extremes), the model differs from the observations. Again, this suggests that the model is better at predicting the lower extremes, likely as that is where more observations are seen.

The fitted GEVD model is then used to predict return values (this is similar to reading off the y value of the orange curve as a function of return period in panel 3(a)). These predicted return values are presented in Figure 3(d) as a function of return period, and with 50% confidence interval widths recorded. Return values describe the magnitude of B which will be exceeded at least once within the associated return period. For example, Valentia B observations will exceed 701 nT (50% CI: -41, +191) at least once in a 20 year period.

3.3 Modelling the distribution of dB/dt extremes

The fitting of the GEVD model to the $\frac{dB}{dt}$ extremes is analysed in Figure 4 as it was for B values. In panel 4(a), the model fits the observations mostly within the confidence interval, except for one outlier at high $\frac{dB}{dt}$. Again in panel 4(b), the model fits the data well at lower $\frac{dB}{dt}$, and this is also true from examination of the QQ plot in panel 4(c). In each of the assessment figures, the GEVD model tends to fit $\frac{dB}{dt}$ data better than it did for B data.

The return values for $\frac{dB}{dt}$ are presented with 50% confidence intervals in the table in panel 4(d). For example, Valentia $\frac{dB}{dt}$ observations will exceed 183.73 nT min⁻¹ (50% CI: -11.98, +53.53) at least once in a 20 year period.

4 Contributions to extreme values

In this section, the values observed at Valentia during geomagnetic storms, substorms and SCs will be compared with the return values extracted from the EVA. The values of B recorded at Valentia during different phases of storms, substorms and sudden commencements are recorded in Figure 5 (an equivalent plot for $\frac{dB}{dt}$ is presented in

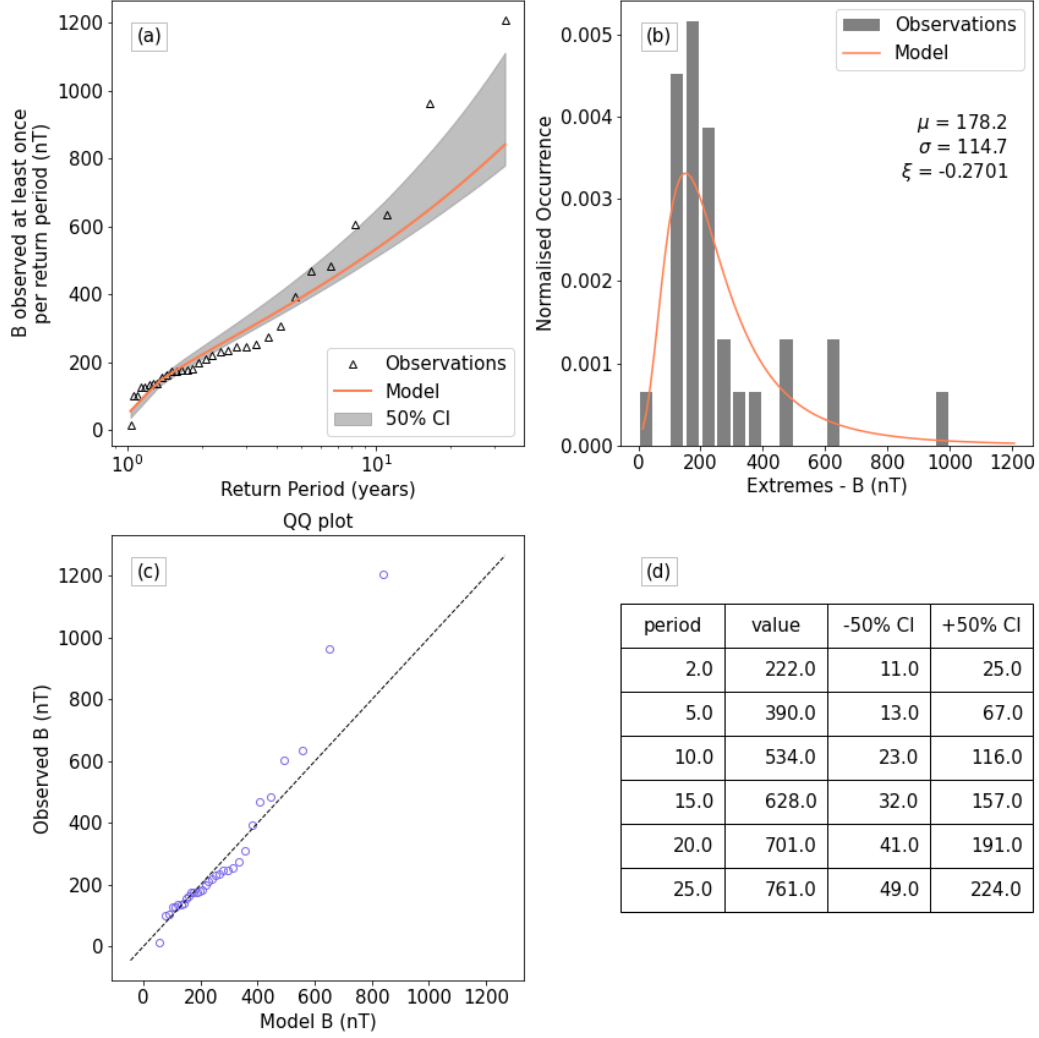


Figure 3. Extreme value analysis for B. (a) Observed extremes as a function of their calculated return periods (triangles), modelled extremes as a function of return period (orange line) with 50% confidence interval (grey shade). (b) Normalised distributions of the detected B extremes (grey bars) and the fitted GEVD model (orange line), with the fitted parameters defined as for Equation 3 noted in the top right. (c) Quantile-quantile plot comparing the distributions of the modelled (x) and observed (y) extremes. (d) Return values ('value') as a function of return period ('period' in years), with the width of a 50% confidence interval.

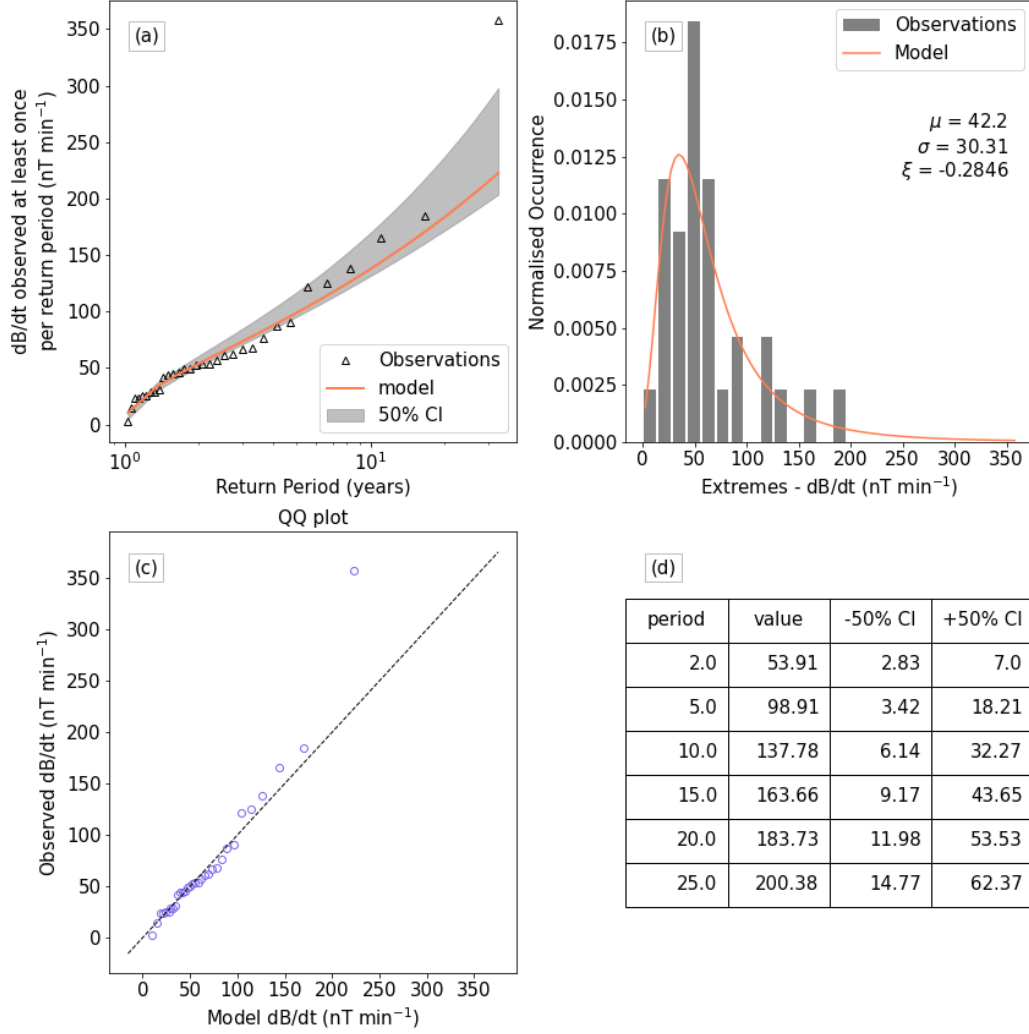


Figure 4. Extreme value analysis for $\frac{dB}{dt}$. (a) Observed extremes as a function of their calculated return periods (triangles), modelled extremes as a function of return period (orange line) with 50% confidence interval (grey shade). (b) Normalised distributions of the detected $\frac{dB}{dt}$ extremes (grey bars) and the fitted GEVD model (orange line), with the fitted parameters defined as for Equation 3 noted in the top right. (c) Quantile-quantile plot comparing the distributions of the modelled (x) and observed (y) extremes. (d) Return values ('value') as a function of return period ('period' in years), with the width of a 50% confidence interval.

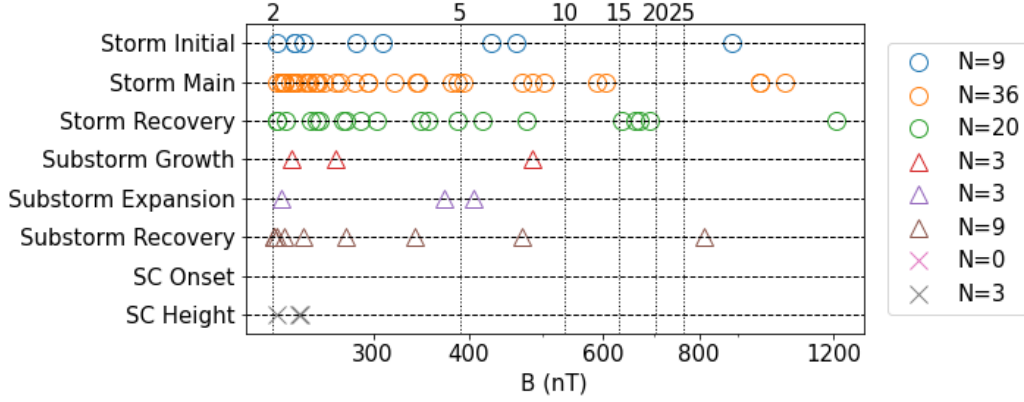


Figure 5. Valentia B values during different event phases. For storms, the maximum value in the labelled phase of each Walach and Grocott (2019) storm between 1991 and 2021. For substorms, the maximum value in each phase (where recovery phase is the 30 mins following recovery start time) for Forsyth et al. (2015) SOPHIE substorms between 1996 and 2014. Finally, for SCs, the onset value is the maximum value between onset time and the end of the SC increase, whereas the height value is the maximum value from the end of the SC increase to 10 minutes afterwards. Only B measurements greater than the 2 year return value of 222.0 nT are plotted. Vertical lines indicate 2, 5, 10, 15, 20 and 25 year return values. Number of points for each category is recording in the legend. Horizontal axis is in log scale.

Figure 6). For storms, the maximum value during initial, main and recovery phase is calculated using the Walach and Grocott (2019) storm list. Similarly for substorms, the maximum value during growth, expansion and recovery phase (where these phases are defined in section 2) from the Forsyth et al. (2015) SOPHIE substorm list. Finally, for SCs, the maximum recorded value for the period between onset and height of the step change (‘onset’) and the height of the step change and the 10 minutes that follow (‘height’) are extracted. For all three event types, only observations which equal or exceed the 2 year return value for B or $\frac{dB}{dt}$ are plotted.

For B values presented in Figure 5, storms contribute a larger number of observations above the 2 year return value than substorms or SCs (notably there are no SC onset observations that exceed the 2 year return value). This is particularly interesting given that there are many more substorms observed than storms: only 314 storms, but over 26,000 substorms. Despite this, all three phases of storms and substorms contribute to high B observations. SC onset does not contribute to high B observations, perhaps since this is the start of the step change that forms an SC, and so the horizontal component of the magnetic field will be at its lowest for this event. Conversely, at SC height, where the magnetic field should be the highest (within the SC time frame), there are three observations above the 2 year return value.

Figure 6 shows the $\frac{dB}{dt}$ values recorded by Valentia during the storms, substorms and SCs which equal or exceed the two year return value. Again, all three phases of storms and substorms contribute to these unusual $\frac{dB}{dt}$ values, while storms however contribute more high $\frac{dB}{dt}$ than substorms. Unlike for B, SC onset rather than height contribute to high $\frac{dB}{dt}$ values. This is likely as the onset period represents the beginning of the step change, so will contain high values of $\frac{dB}{dt}$ due to the nature of the change. The height portion comes from values following the step change, so may not contribute to high $\frac{dB}{dt}$ values. It is important to note at this point that ULF waves or related field-line reso-

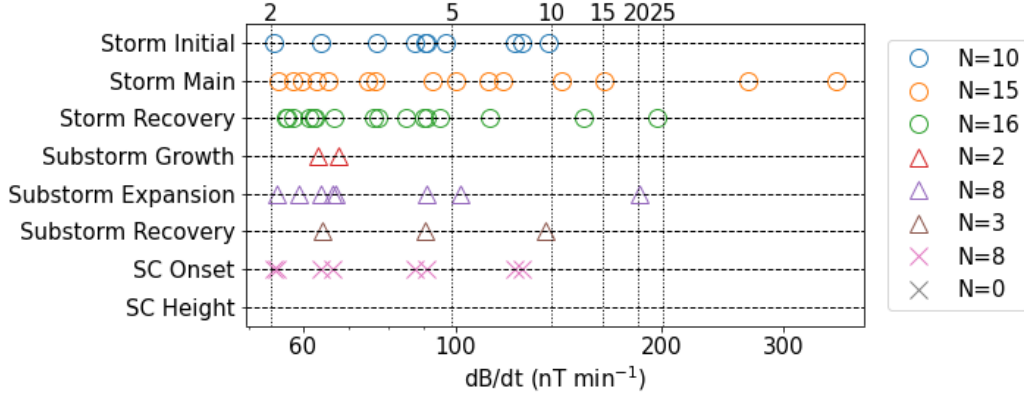


Figure 6. Valentia $\frac{dB}{dt}$ values during different event phases. For storms, the maximum value in the labelled phase of each Walach and Grocott (2019) storm between 1991 and 2021. For substorms, the maximum value in each phase (where recovery phase is the 30 mins following recovery start time) for Forsyth et al. (2015) SOPHIE substorms between 1996 and 2014. Finally, for SCs, the onset value is the maximum value between onset time and the end of the SC increase, whereas the height value is the maximum value from the end of the SC increase to 10 minutes afterwards. Only $\frac{dB}{dt}$ measurements greater than the 2 year return value of 53.88 nT min⁻¹ are plotted. Vertical lines indicate 2, 5, 10, 15, 20 and 25 year return values. Number of points for each category is recording in the legend. Horizontal axis is in log scale.

nances may contribute to high $\frac{dB}{dt}$ values, but the minute resolution of Valentia data is not fine enough to capture these rapid changes; further investigation with higher resolution data is necessary to determine to what extent wave activity contributes to high $\frac{dB}{dt}$ values.

An interesting point to consider in this analysis is that substorms may occur during storms, and so some of the B and $\frac{dB}{dt}$ values in the storm and substorm phases may come from similar intervals. However, the aim of this analysis was to characterise the contributions different events make to extreme values, and separating events into storms with/without substorms is out of the scope of this study.

Finally, the extreme value analysis technique (as applied to B and $\frac{dB}{dt}$) is applied to various IMF, solar wind characteristics and geomagnetic indices, using data between 1991 and 2021 inclusive. These results are summarised in Table 1. Rather than an in depth analysis as for B and $\frac{dB}{dt}$, for brevity the distribution and fit parameters are presented, along with the return values for 2, 5, 10, 15, 20 and 25 years. These return values will be used to assess the rarity of the conditions that generate the extreme B value presented in Figure 1. Guided by the distributions presented by Fogg et al. (2022), the EVA is run over block minima (i.e. negative maxima) for AL and SYM-H. This also links to negative signatures in AL generated by substorms, and negative signatures in SYM-H relating to geomagnetic storms. Finally, it is important to note that solar cycle variations in solar wind, IMF and geomagnetic indices have not been removed in this analysis: the purpose of this analysis is to assess the rarity of observations in Figure 1, and hence which parameters are driving the observed B extreme.

Note that the EVA was not applied to B_Y , B_Z or PC_N as these parameters are roughly equally likely to be positive or negative (following on from the distributions presented by Fogg et al. (2022)), and the geophysical meaning of these different signs is significant. For example, positive PC_N indicates Dungey driven dual cell convection, whereas

Table 1. Fit parameters and return values for EVA analysis of various IMF, solar wind characteristics and geomagnetic indices; left hand column denotes the parameter. Distribution indicates whether the GEVD or Gumbel distribution was fitted; both are fitted using MCMC as for B and $\frac{dB}{dt}$. μ , σ and ξ denote the free parameters in the fitting. Columns 2, 5, 10, 15, 20 and 25 denote the return values for the titular return period in years.

	Distribution	μ	σ	ξ	2	5	10	15	20	25
B_{TOTAL} (nT)	Gumbel	30.8	11.5	0.00	35.0	48.0	57.0	62.0	65.0	68.0
V_{SW} (km s ⁻¹)	Gumbel	833.4	96.5	0.00	869.0	978.0	1051.0	1091.0	1120.0	1142.0
P_{SW} (nPa)	GEVD	28.5	12.0	-0.37	33.0	52.0	70.0	83.0	93.0	102.0
AE (nT)	Gumbel	2345.7	641.0	0.00	2581.0	3307.0	3788.0	4059.0	4250.0	4396.0
AU (nT)	Gumbel	819.4	314.1	0.00	935.0	1291.0	1526.0	1659.0	1752.0	1824.0
AL (nT)	Gumbel	-247.7	646.6	0.00	-2339.0	-3072.0	-3557.0	-3831.0	-4023.0	-4170.0
SYM-H (nT)	Gumbel	137.0	91.4	0.00	-181.0	-284.0	-353.0	-391.0	-419.0	-439.0

negative PC_N may indicate reverse convection or a severe asymmetry in the convection pattern. Although different signs of B_Y relate to opposite asymmetries in magnetospheric and ionospheric signatures, some magnitude of either sign may increase energy input from the solar wind (e.g., Grocott et al., 2003, 2004, 2008); however interpretation of, for example, the return period of the magnitude of B_Y would be non-trivial. Finally, for IMF B_Z , the difference between positive and negative represents a fundamental difference in the energy transfer between the solar wind and magnetosphere - the difference between a Dungey cycle-driven magnetosphere prone to storms and substorms, and a magnetosphere moving towards a more closed state (e.g., Milan et al., 2020, 2022). Due to the necessity for a long and approximately continuous dataset, the timeseries cannot be split into two positive and negative counterparts.

In the example presented in Figure 1, B_{TOTAL} is fairly steady around 50 nT throughout the interval, driven by a dominant IMF B_Y ; according to the return values presented in Table 1 this is between a 5 and 10 year event. The solar wind flow speed is greater than 1050 km s⁻¹ at the time of the B extreme, between a 10 and 15 year event according to Table 1. The flow pressure varies between 10 and 30 nPa through the presented interval surrounding the B maximum. The 2 year return value of flow pressure is 33 nPa, so since the pressure is often below this value it is likely not driving the extreme observations in B.

Both AL and AE do not reach the their two year return values in the presented interval, observed at around -500 and +1000 nT respectively. AU however exceeds the 2 year return value, suggesting that perhaps this interval is dominated by moderate-strong dayside driving, rather than nightside substorm driving characteristic of AL. Finally, in Figure 1, SYM-H is around -300 nT, between the 5 and 10 year return values, and far below the quiet threshold (Walach & Grocott, 2019). Bergin et al. (2023) performed EVA on Dst, SYM-H and SMR, and the calculated 5 and 10 year return values are within their confidence intervals for the same return values (see Table 2 of Bergin et al. (2023)).

In the B extreme presented in Figure 1, IMF B_{TOTAL} , V_{SW} , and SYM-H are exhibiting between 5 and 10 year values. Considering the lack of characteristic substorm signatures in AL, and a long period of southward IMF, results from Table 1 suggest the B extreme is driven by a once in 5/10 year geomagnetic storm, incorporating strong solar wind driving in particular from V_{SW} .

5 Conclusion

Investigation of space weather effects on Ireland is at an early stage when compared with other geographical areas, with the majority of this research utilising the MagIE network of magnetometers. In this study, extreme events at the MagIE station at Valentia have been identified as the peak value observed in a calendar year. A GEVD model was fitted to these data via MCMC fitting, and from this model return values at given return periods are extracted. This process was repeated for both the horizontal component of the magnetic field, B , and its time derivative, $\frac{dB}{dt}$. Understanding the return values at Valentia provides a window onto space weather effects at Ireland, which is becoming increasingly important as the world moves towards a more technologically dependent society.

Additionally, the MLT distribution of the detected extremes was examined. As Ireland moves from day to night, the Valentia magnetometer rotates in and out of view of different regions of the magnetosphere, which can be dominated by different phenomena. More extremes were detected at premidnight MLTs, linking back to the dominance of substorm dynamics in the premidnight sector, and the dramatic bay-like features observed in magnetometer observations. Also presented in this study was an extreme in B , in a period with a strong B_{TOTAL} , and dominated by a 5-10 year storm.

Open Research Section

Data from Valentia MagIE station was obtained via the SuperMAG archive: <https://supermag.jhuapl.edu/>. SuperMAG is made possible by the generous funding provided by the National Science Foundation (NSF) and National Aeronautics and Space Administration (NASA). We gratefully acknowledge: NSF ATM-0646323, NSF AGS-1003580, NASA NNX08AM32G S03. We gratefully acknowledge the SuperMAG collaborators (<http://supermag.jhuapl.edu/info/?page=acknowledgement>) (Gjerlov, 2012). SuperMAG indices SME/SMU/SML (Newell & Gjerloev, 2011) and SMR (Newell & Gjerloev, 2012) were obtained from: <https://supermag.jhuapl.edu/indices/>.

We gratefully acknowledge use of NASA/GSFC's Space Physics Data Facility's OMNIWeb (<https://omniweb.gsfc.nasa.gov/hw.html>) service, and OMNI data (Papitashvili, N., 2023). The AE and SYM-H indices used in this paper were provided by the WDC for Geomagnetism, Kyoto (<http://wdc.kugi.kyoto-u.ac.jp/wdc/Sec3.html>) via OMNIWeb. PC(N) index was provided by World Data Center for Geomagnetism, Copenhagen via OMNIWeb.

A subset of Walach and Grocott (2019) storms are available in the supporting information of Walach and Grocott (2019) at: <https://agupubs.onlinelibrary.wiley.com/doi/10.1029/2019JA026816>. The SOPHIE substorm list is available in the supporting information of Forsyth et al. (2015) at: <https://agupubs.onlinelibrary.wiley.com/doi/full/10.1002/2015JA021343>. The sudden commencement event list used in this paper was compiled by Observatori de l'Ebre (2020). Events are freely available from: <https://www.obsebre.es/en/rapid>.

The authors gratefully acknowledge the use of the `pyextremes` python package: <https://pypi.org/project/pyextremes/>. The authors also gratefully acknowledge the use of the `emcee` python package: <https://pypi.org/project/emcee/> by Foreman-Mackey et al. (2013).

Acknowledgments

ARF's work was supported by Irish Research Council Government of Ireland Postdoctoral Fellowship GOIPD/2022/782. CMJ's work was supported by the Science Foundation Ireland Grant 18/FRL/6199. JM-L was supported by the Irish Research Council.

AWS was supported by NERC Independent Research Fellowship NE/W009129/1. MTW was supported by the UKRI Natural Environment Research Council Grant NE/T000937/1. ML is support by the UK Science, Technology and Facilities Council grant ST/W00089X/1. JEW was supported by a CNES postdoctoral fellowship.

References

- Akaike, H. (1974). A new look at the statistical model identification. *IEEE Transactions on Automatic Control*, 19(6), 716–723. doi: 10.1109/TAC.1974.1100705
- Araki, T. (1994). A physical model of the geomagnetic sudden commencement. *Geophysical Monograph*, 81, 183–200. doi: 10.1029/GM081p0183
- Bergin, A., Chapman, S. C., & Gjerloev, J. W. (2020). AE, Dst, and their SuperMAG counterparts: The effect of improved spatial resolution in geomagnetic indices. *Journal of Geophysical Research: Space Physics*, 125(e2020JA027828). doi: 10.1029/2020JA027828
- Bergin, A., Chapman, S. C., Watkins, N. W., Moloney, N. R., & Gjerloev, J. W. (2023). Extreme event statistics in Dst, SYM-H, and SMR geomagnetic indices. *Space Weather*, 21(e2022SW003304). doi: 10.1029/2022SW003304
- Blake, S. P., Gallagher, P. T., Campaña, J., Hogg, C., Beggan, C., Thomson, A. W. P., ... Bell, D. (2018). A detailed model of the irish high voltage power network for simulating gics. *Space Weather*, 16, 1770–1783. doi: 10.1029/2018SW001926
- Blake, S. P., Gallagher, P. T., McCauley, J., Jones, A. G., Hogg, C., Campaña, J., ... Bell, D. (2016). Geomagnetically induced currents in the irish power network during geomagnetic storms. *Space Weather*, 14, 1136–1154. doi: 10.1002/2016SW001534
- Bolduc, L. (2002). GIC observations and studies in the Hydro-Québec power system. *Journal of Atmospheric and Solar-Terrestrial Physics*, 64, 1793–1802. doi: 10.1016/S1364-6826(02)00128-1
- Bristow, W. A., & Jensen, P. (2007). A superposed epoch study of SuperDARN convection observations during substorms. *Journal of Geophysical Research: Space Physics*, 112(A6). doi: 10.1029/2006JA012049
- Bristow, W. A., Otto, A., & Lummerzheim, D. (2001). Substorm convection patterns observed by the Super Dual Auroral Radar Network. *Journal of Geophysical Research: Space Physics*, 106(A11), 24593–24609. doi: 10.1029/2001JA000117
- Bristow, W. A., Sofko, G. J., Stenbaek-Nielsen, H. C., Wei, S., Lummerzheim, D., & Otto, A. (2003). Detailed analysis of substorm observations using SuperDARN, UVI, ground-based magnetometers, and all-sky imagers. *Journal of Geophysical Research: Space Physics*, 108(A3). doi: 10.1029/2002JA009242
- Campaña, J., Gallagher, P. T., Blake, S. P., Gibbs, M., Jackson, D., Beggan, C. D., ... Hogg, C. (2019). Modeling geoelectric fields in ireland and the uk for space weather. *Space Weather*, 216–237. doi: 10.1029/2018SW001999
- Davis, T. N., & Sugiura, M. (1966). Auroral electrojet activity index AE and its universal time variations. *Journal of Geophysical Research*, 71(3), 785–801. doi: 10.1029/JZ071i003p00785
- Elvidge, S. (2020). Estimating the occurrence of geomagnetic activity using the Hilbert-Huang transform and extreme value theory. *Space Weather*, 17(e2020SW002513). doi: 10.1029/2020SW002513
- Fang, T.-W., Kubaryk, A., Goldstein, D., Li, Z., Fuller-Rowell, T., Millward, G., ... Babcock, E. (2022). Space weather environment during the SpaceX Starlink satellite loss in February 2022. *Space Weather*, 20(e2022SW003193). doi: 10.1029/2022SW003193
- Finkel, J., Gerber, E. P., Abbot, D. S., & Weare, J. (2023). Revealing the Statistics of Extreme Events Hidden in Short Weather Forecast Data. *AGU Advances*,

- 4(e2023AV000881). doi: 10.1029/2023AV000881
- Fogg, A. R. (2021). *SuperDARN Observations of High Latitude Electrodynamics in the Terrestrial Ionosphere* (Doctoral dissertation, University of Leicester School of Physics and Astronomy). doi: 10.25392/leicester.data.16621912.v1
- Fogg, A. R., Jackman, C. M., Waters, J. E., Bonnín, X., Lamy, L., Cecconi, B., ... Louis, C. K. (2022). Wind/WAVES Observations of Auroral Kilometric Radiation: Automated Burst Detection and Terrestrial Solar Wind - Magnetosphere Coupling Effects. *Journal of Geophysical Research: Space Physics*, 127(e2021JA030209). doi: 10.1029/2021JA030209
- Fogg, A. R., Lester, M., Yeoman, T. K., Carter, J. A., Milan, S. E., Sangha, H. K., ... Vines, S. K. (2023). Multi-instrument observations of the effects of a solar wind pressure pulse on the high latitude ionosphere: a detailed case study of a geomagnetic sudden impulse. *Journal of Geophysical Research: Space Physics*, 128(e2022JA031136). doi: 10.1029/2022JA031136
- Foreman-Mackey, D., Hogg, D. W., Lang, D., & Goodman, J. (2013). emcee: The MCMC Hammer. *Publications of the Astronomical Society of the Pacific*, 125(925), 306. doi: 10.1086/670067
- Forsyth, C., Rae, I. J., Coxon, J. C., Freeman, M. P., Jackman, C. M., Gjerloev, J., & Fazakerley, A. N. (2015). A new technique for determining Substorm Onsets and Phases from Indices of the Electrojet (SOPHIE). *Journal of Geophysical Research: Space Physics*, 120, 10592–10606. doi: 10.1002/2015JA021343
- Freeman, M. P., Forsyth, C., & Rae, I. J. (2019). The Influence of Substorms on Extreme Rates of Change of the Surface Horizontal Magnetic Field in the United Kingdom. *Space Weather*, 17(6). doi: 10.1029/2018SW002148
- Gillies, D. M., St. Maurice, J. P., McWilliams, K. A., & Milan, S. (2012). Global-scale observations of ionospheric convection variation in response to sudden increases in the solar wind pressure. *Journal of Geophysical Research: Space Physics*, 117(A4). doi: 10.1029/2011JA017255
- Gjerlov, J. W. (2012). The SuperMAG data processing technique. *Journal of Geophysical Research*(A09213). doi: 10.1029/2012JA017683
- Grocott, A., Badman, S. V., Cowley, S. W. H., Yeoman, T. K., & Cripps, P. J. (2004). The influence of IMF By on the nature of the nightside high-latitude ionospheric flow during intervals of positive IMF Bz. *Annales Geophysicae*, 22(5), 1755–1764. doi: 10.5194/angeo-22-1755-2004
- Grocott, A., Cowley, S. W. H., & Sigwarth, J. B. (2003). Ionospheric flow during extended intervals of northward but By-dominated IMF. *Annales Geophysicae*, 21(2), 509–538. doi: 10.5194/angeo-21-509-2003
- Grocott, A., Milan, S. E., & Yeoman, T. K. (2008). Interplanetary magnetic field control of fast azimuthal flows in the nightside high-latitude ionosphere. *Geophysical Research Letters*, 35(8). doi: 10.1029/2008GL033545
- Hori, T., Shinbori, A., Fujita, S., & Nishitani, N. (2015). IMF-By dependence of transient ionospheric flow perturbation associated with sudden impulses: SuperDARN observations. *Earth, Planets and Space*, 67(190). doi: 10.1186/s40623-015-0360-6
- Hutchinson, J. A., Wright, D. M., & Milan, S. E. (2011). Geomagnetic storms over the last solar cycle: A superposed epoch analysis. *Journal of Geophysical Research: Space Physics*, 116(A9). doi: 10.1029/2011JA016463
- Hutchinson, J. A., Wright, D. M., Milan, S. E., Grocott, A., & Boakes, P. D. (2011). A new way to study geomagnetic storms. *Astronomy and Geophysics*, 52(4). doi: 10.1111/j.1468-4004.2011.52420.x
- Iyemori, T. (1990). Storm-Time Magnetospheric Currents Inferred from Mid-Latitude Geomagnetic Field Variations. *Journal of Geomagnetism and Geoelectricity*, 42(11), 1249–1265. doi: 10.5636/jgg.42.1249
- King, J. H., & Papitashvili, N. E. (2005). Solar wind spatial scales in and comparisons of hourly Wind and ACE plasma and magnetic field data. *Journal of*

- Geophysical Research: Space Physics*, 110(A2). doi: 10.1029/2004JA010649
- Koons, H. C. (2001). Statistical analysis of extreme values in space science. *Journal of Geophysical Research*, 106(A6), 10915–10921. doi: 10.1029/2000JA000234
- Malone-Leigh, J., Campanyà, J., Gallagher, P. T., Neukirch, M., Hogg, C., & Hoggson, J. (2023). Nowcasting geoelectric fields in ireland using magnetotelluric transfer functions. *Journal of Space Weather and Space Climate*. doi: 10.1051/swsc/2023004
- McPherron, R. L. (1970). Growth phase of magnetospheric substorms. *Journal of Geophysical Research: Space Physics*, 75(28). doi: 10.1029/JA075i028p05592
- McPherron, R. L. (1995). Magnetospheric dynamics. In M. G. Kivelson & C. T. Russell (Eds.), *Introduction to space physics* (p. 400-458). Cambridge University Press.
- Milan, S. E., Bower, G. E., Carter, J. A., Paxton, L. J., Anderson, B. J., & Hairston, M. R. (2022). Lobe reconnection and cusp-aligned auroral arcs. *Journal of Geophysical Research: Space Physics*, 127(e2021JA030089). doi: 10.1029/2021JA030089
- Milan, S. E., Carter, J. A., Bower, G. E., Imber, S. M., Paxton, L. J., Anderson, B. J., ... Hubert, B. (2020). Dual-Lobe Reconnection and Horse-Collar Auroras. *Journal of Geophysical Research: Space Physics*, 125(e2020JA028567). doi: 10.1029/2020JA028567
- Newell, P. T., & Gjerloev, J. W. (2011). Evaluation of SuperMAG auroral electrojet indices as indicators of substorms and auroral power. *Journal of Geophysical Research: Space Physics*, 116(A12211). doi: 10.1029/2011JA016779
- Newell, P. T., & Gjerloev, J. W. (2012). SuperMAG-based partial ring current indices. *Journal of Geophysical Research: Space Physics*, 117(A05215). doi: 10.1029/2012JA017586
- Nishimura, Y., Lyons, L. R., Gabrielse, C., Sivadas, N., Donovan, E. F., & Varney, R. H. (2020). Extreme magnetosphere-ionosphere-thermosphere response to the 5 April 2010 supersubstorm. *Journal of Geophysical Research: Space Physics*, 125(e2019JA027654). doi: 10.1029/2019JA027654
- Observatori de l'Ebre. (2020). *International service on rapid magnetic variations*. Retrieved from <http://www.obsebre.es/en/rapid> (Accessed on: 07-02-2020)
- Oliveira, D. M., Hartinger, M. D., Xi, Z., Zesta, E., Pilipenko, V. A., Giles, B. L., & Silveira, M. V. D. (2020). Interplanetary Shock Impact Angles Control Magnetospheric ULF Wave Activity: Wave Amplitude, Frequency, Power Spectra. *Geophysical Research Letters*, 47(24). doi: 10.1029/2020GL090857
- Orr, L., Grocott, A., Walach, M.-T., Chisham, G., Freeman, M. P., Lam, M. M., & Shore, R. M. (2023). A quantitative comparison of high latitude electric field models during a large geomagnetic storm. *Space Weather*, 21(1), e2022SW003301. doi: <https://doi.org/10.1029/2022SW003301>
- Papitashvili, N. (2023). *Omniweb plus*. Retrieved from <https://omniweb.gsfc.nasa.gov/hw.html> ([Dataset])
- Riley, P., & Love, J. J. (2017). Extreme geomagnetic storms: Probabilistic forecasts and their uncertainties. *Space Weather*, 15, 53–64. doi: 10.1002/2016SW001470
- Rogers, N. C., Wild, J. A., Eastoe, E. F., Gjerloev, J. W., & Thomson, A. W. P. (2020). A global climatological model of extreme geomagnetic field fluctuations. *Journal of Space Weather and Space Climate*, 10(5). doi: 10.1051/swsc/2020008
- Sandhu, J. K., Rae, I. J., Wygant, J. R., Breneman, A. W., Tian, S., Watt, C. E. J., ... Walach, M.-T. (2021). Ulf wave driven radial diffusion during geomagnetic storms: A statistical analysis of van allen probes observations. *Journal of Geophysical Research: Space Physics*, 126(4), e2020JA029024. doi: <https://doi.org/10.1029/2020JA029024>

- Sangha, H., Milan, S. E., Carter, J. A., Fogg, A. R., Anderson, B. J., Korth, H., & Paxton, L. J. (2020). Bifurcated Region 2 Field-Aligned Currents Associated With Substorms. *Journal of Geophysical Research: Space Physics*, 125(1). doi: 10.1029/2019JA027041
- Silbergleit, V. M. (1996). On the Occurrence of Geomagnetic Storms with Sudden Commencements. *Journal of Geomagnetism and Geoelectricity*, 48, 1011–1016. doi: 10.5636/jgg.48.1011
- Silbergleit, V. M. (1999). Forecast of the most geomagnetically disturbed days. *Earth, Planets, Space*, 51, 19–22. doi: 10.1186/BF03352205
- Siscoe, G. L. (1976). On the statistics of the largest geomagnetic storms per solar cycle. *Journal of Geophysical Research*, 81(25), 4782–4784. doi: 10.1029/JA081i025p04782
- Smith, A. W., Forsyth, C., Rae, J., Rodger, C. J., & Freeman, M. P. (2021). The impact of sudden commencements on ground magnetic field variability: Immediate and delayed consequences. *Space Weather*, 19(e2021SW002764). doi: 10.1029/2021SW002764
- Smith, A. W., Freeman, M. P., Rae, I. J., & Forsyth, C. (2019). The influence of sudden commencements on the rate of change of the surface horizontal magnetic field in the united kingdom. *Space Weather*, 17, 1605–1617. doi: 10.1029/2019SW002281
- Smith, A. W., Jackman, C. M., Frohmaier, C. M., Coxon, J. C., Slavin, J. A., & Fear, R. C. (2018). Evaluating Single-Spacecraft Observations of Planetary Magnetotails With Simple Monte Carlo Simulations: 1. Spatial Distributions of the Neutral Line. *Journal of Geophysical Research: Space Physics*, 123(10). doi: 10.1029/2018JA025958
- Stauning, P. (2013). The Polar Cap index: A critical review of methods and a new approach. *Journal of Geophysical Research: Space Physics*, 118, 5021–5038. doi: 10.1002/jgra.50462
- Thomson, A. W. P., Dawson, E. B., & Reay, S. J. (2011). Quantifying extreme behaviour in geomagnetic activity. *Space Weather*, 9(S10001). doi: 10.1029/2011SW000696
- Troshichev, O. A., & Andrezen, V. G. (1985). The relationship between interplanetary quantities and magnetic activity in the southern polar cap. *Planetary Space Science*, 33(4), 415–419. doi: 10.1016/0032-0633(85)90086-8
- Troshichev, O. A., Dmitrieva, N. P., & Kuznetsov, B. M. (1979). Polar cap magnetic activity as a signature of substorm development. *Planetary and Space Science*, 27(3), 217–221. doi: 10.1016/0032-0633(79)90063-1
- Tsubouchi, K., & Omura, Y. (2007). Long-term occurrence probabilities of intense geomagnetic storm events. *Space Weather*, 5(S12003). doi: 10.1029/2007SW000329
- Walach, M.-T., & Grocott, A. (2019). SuperDARN Observations During Geomagnetic Storms, Geomagnetically Active Times and Enhanced Solar Wind Driving. *Journal of Geophysical Research: Space Physics*, 124(7), 5828–5847. doi: 10.1029/2019JA026816
- Waters, J. E., Jackman, C. M., Whiter, D., Forsyth, C., Fogg, A. R., Lamy, L., ... Issautier, K. (2022). A perspective on substorm dynamics using 10 years of Auroral Kilometric Radiation observations from Wind. *Journal of Geophysical Research: Space Physics*(9), 127. doi: 10.1029/2022JA030449
- Weimer, D. R., & King, J. H. (2008). Improved calculations of interplanetary magnetic field phase front angles and propagation time delays. *Journal of Geophysical Research: Space Physics*, 113(A1). doi: 10.1029/2007JA012452
- Weimer, D. R., Ober, D. M., Maynard, N. C., Burke, W. J., Collier, M. R., McComas, D. J., ... Smith, C. W. (2002). Variable time delays in the propagation of the interplanetary magnetic field. *Journal of Geophysical Research: Space Physics*, 107(A8). doi: 10.1029/2001JA009102

- 736 Weimer, D. R., Ober, D. M., Maynard, N. C., Collier, M. R., McComas, D. J.,
737 Ness, N. F., ... Watermann, J. (2003). Predicting interplanetary mag-
738 netic field (IMF) propagation delay times using the minimum variance
739 technique. *Journal of Geophysical Research: Space Physics*, 108(A1). doi:
740 10.1029/2002JA009405
- 741 Wharton, S. J., Rae, I. J., Sandhu, J. K., Walach, M.-T., Wright, D. M., & Yeoman,
742 T. K. (2020). The changing eigenfrequency continuum during geomagnetic
743 storms: Implications for plasma mass dynamics and ulf wave coupling. *Jour-*
744 *nal of Geophysical Research: Space Physics*, 125(6), e2019JA027648. doi:
745 <https://doi.org/10.1029/2019JA027648>
- 746 World Data Center for Geomagnetism Kyoto, Nose, M., Iyemori, T., Sugiura,
747 M., & Kamei, T. (2015). *Geomagnetic AE index*. Retrieved from
748 <https://doi.org/10.17593/15031-54800>

Figure 1.

2000-07-15 22:28:00 | 633.8 nT

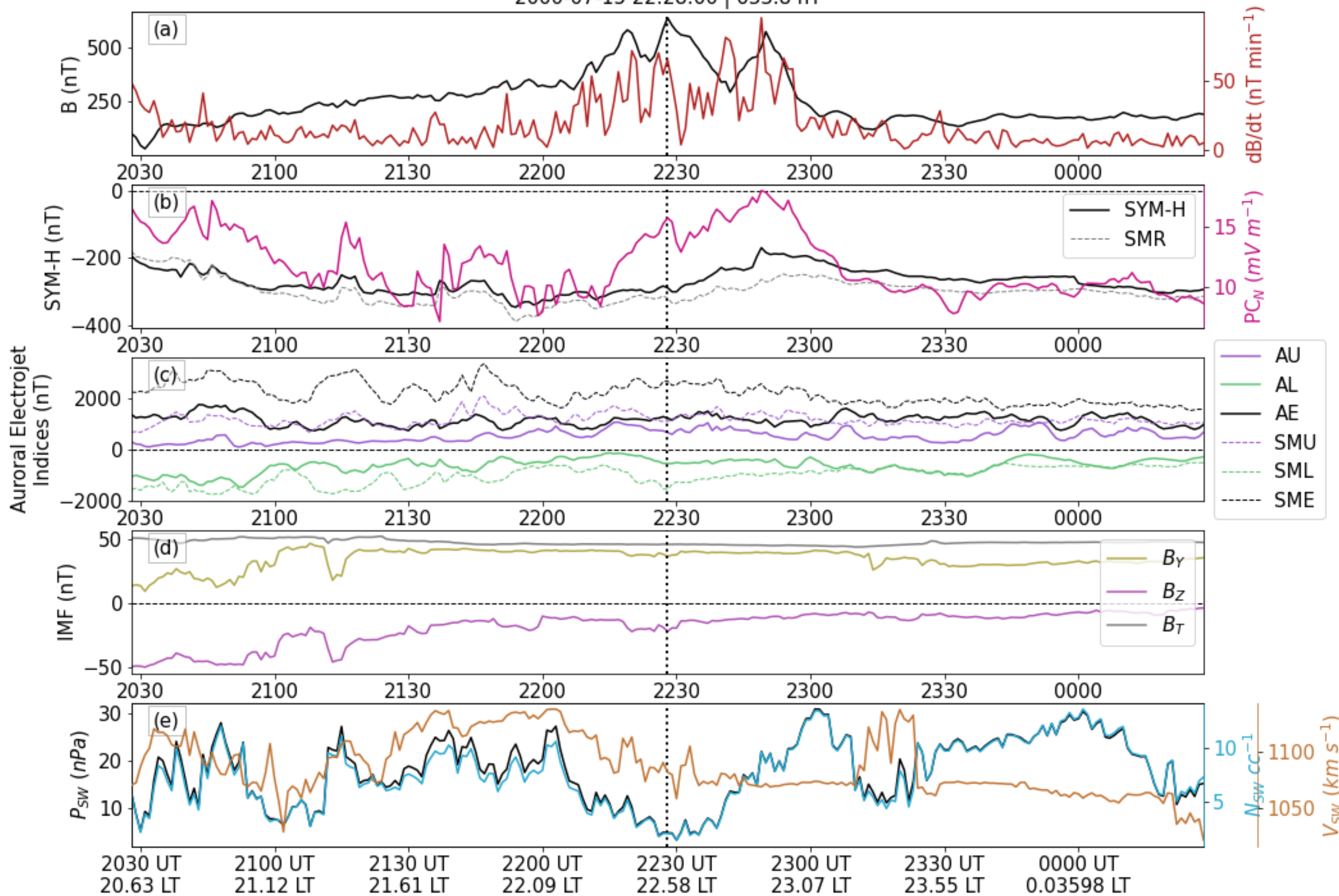


Figure 2.

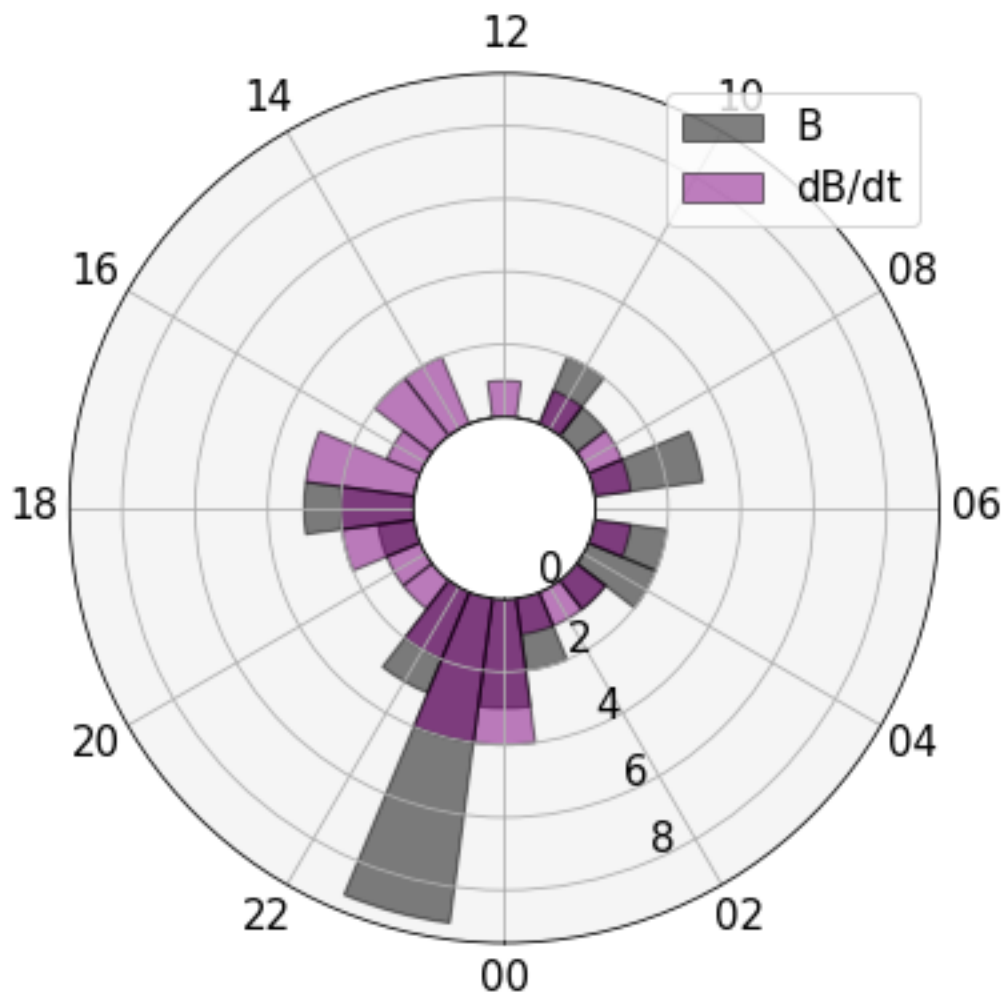
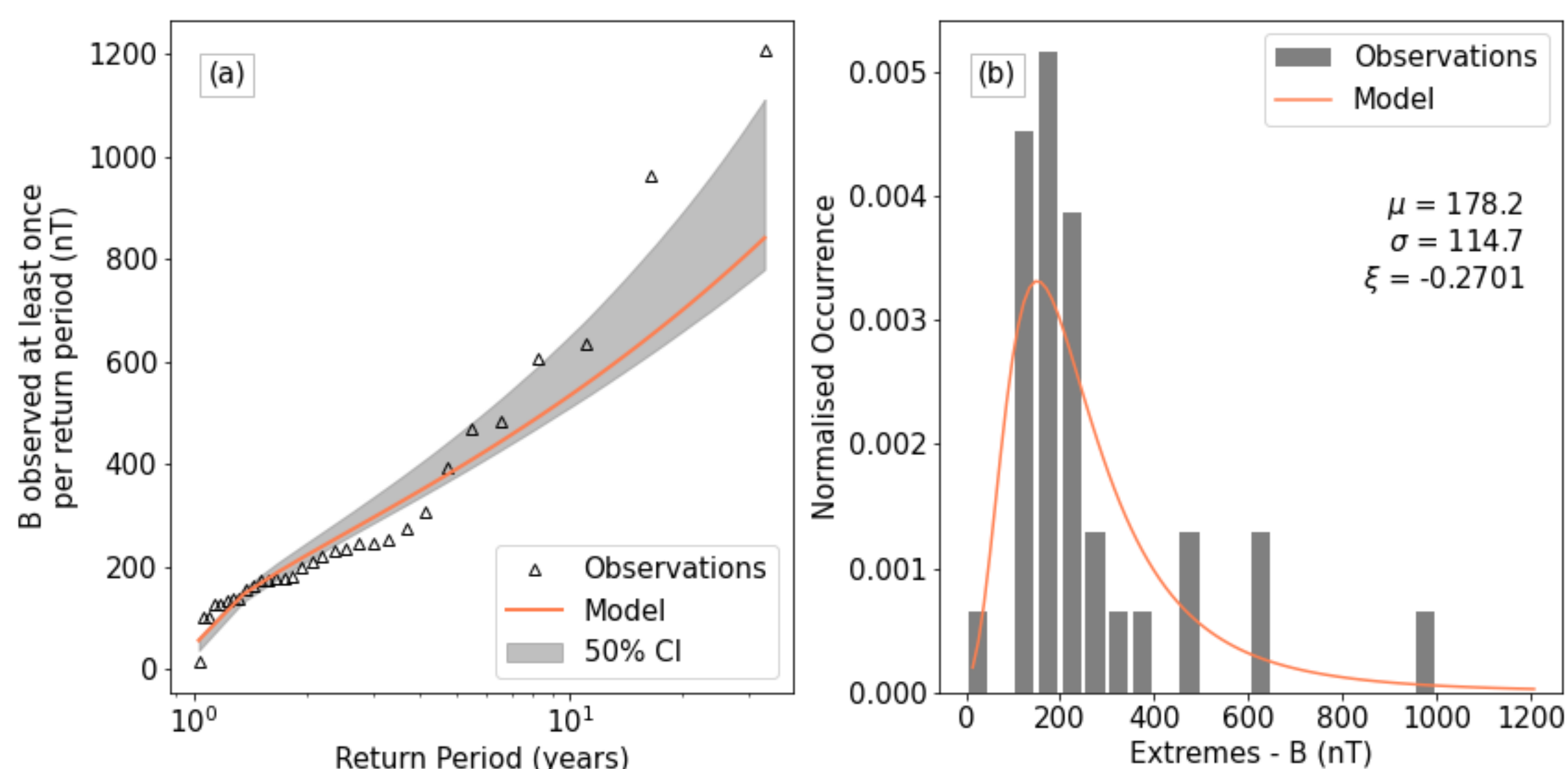
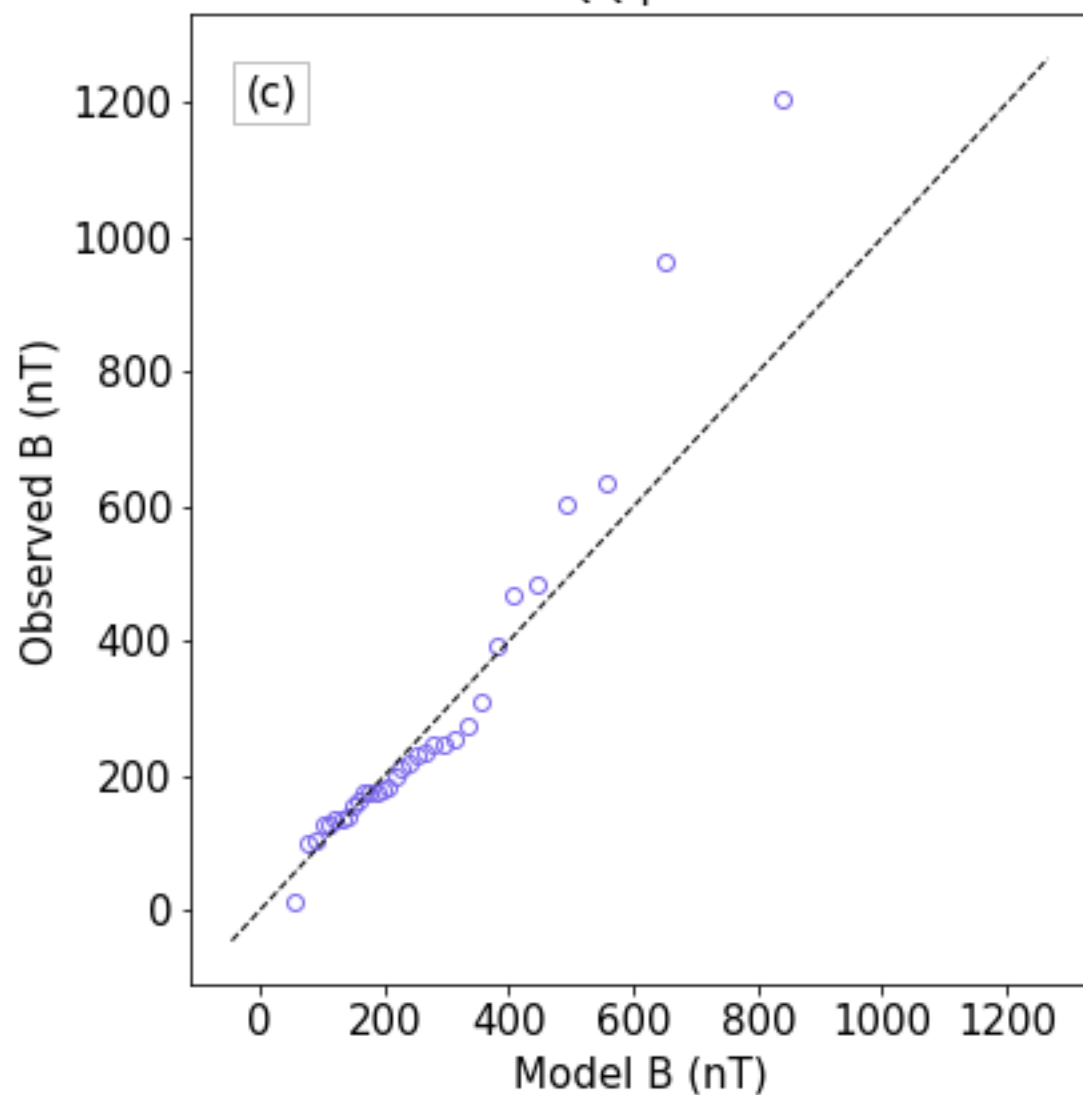


Figure 3.



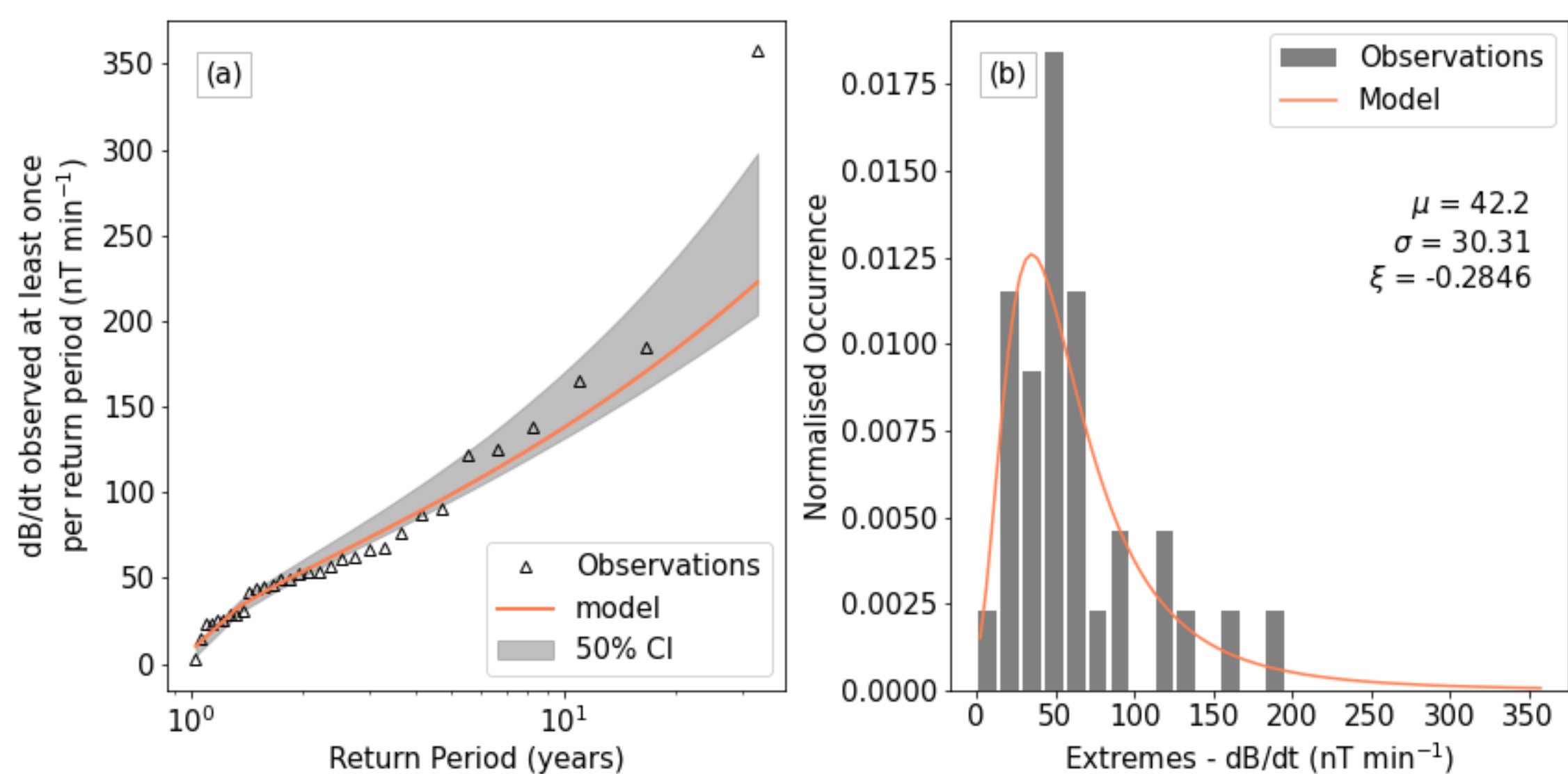
QQ plot



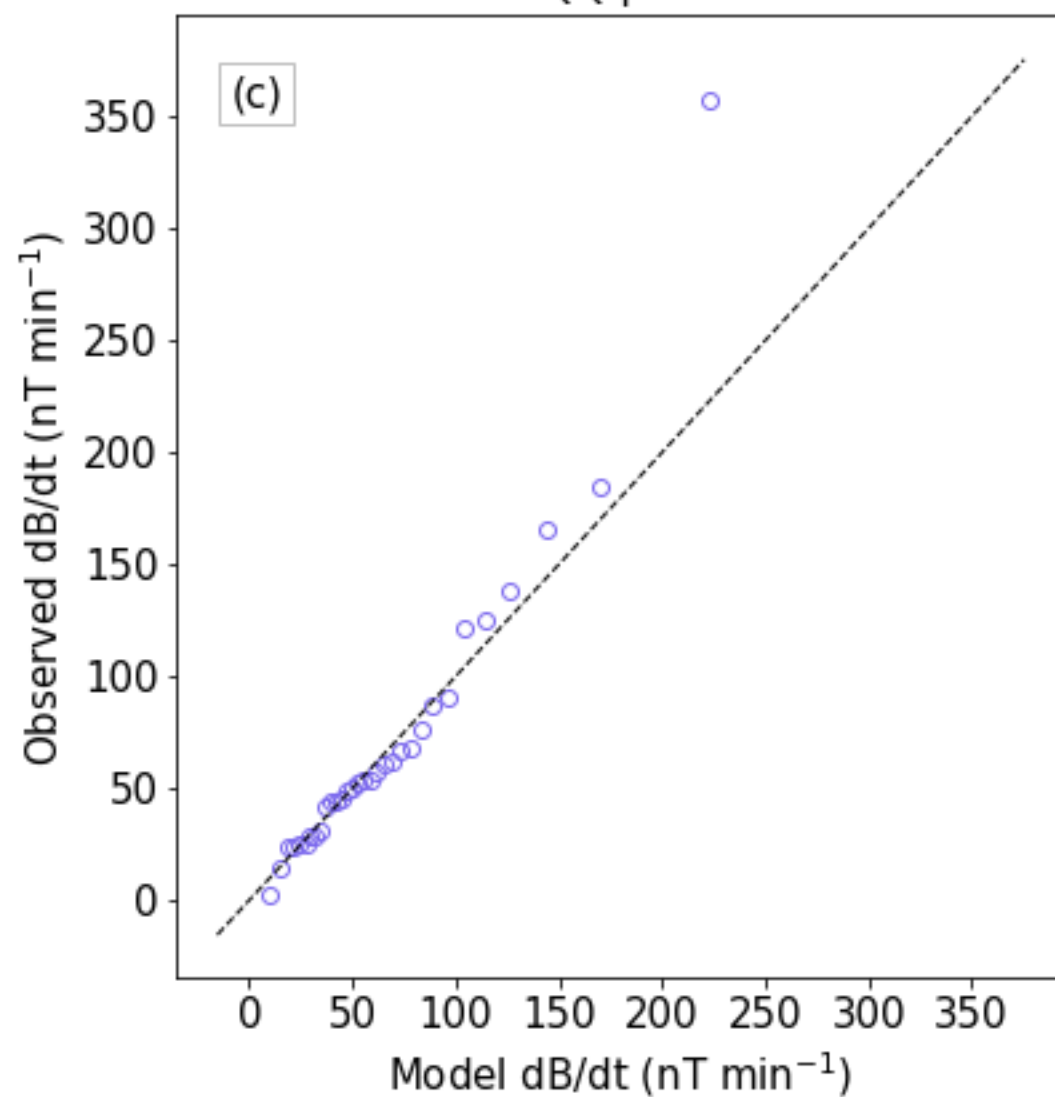
(d) Table of model results for different return periods.

period	value	-50% CI	+50% CI
2.0	222.0	11.0	25.0
5.0	390.0	13.0	67.0
10.0	534.0	23.0	116.0
15.0	628.0	32.0	157.0
20.0	701.0	41.0	191.0
25.0	761.0	49.0	224.0

Figure 4.



QQ plot



(d)

period	value	-50% CI	+50% CI
2.0	53.91	2.83	7.0
5.0	98.91	3.42	18.21
10.0	137.78	6.14	32.27
15.0	163.66	9.17	43.65
20.0	183.73	11.98	53.53
25.0	200.38	14.77	62.37

Figure 5.

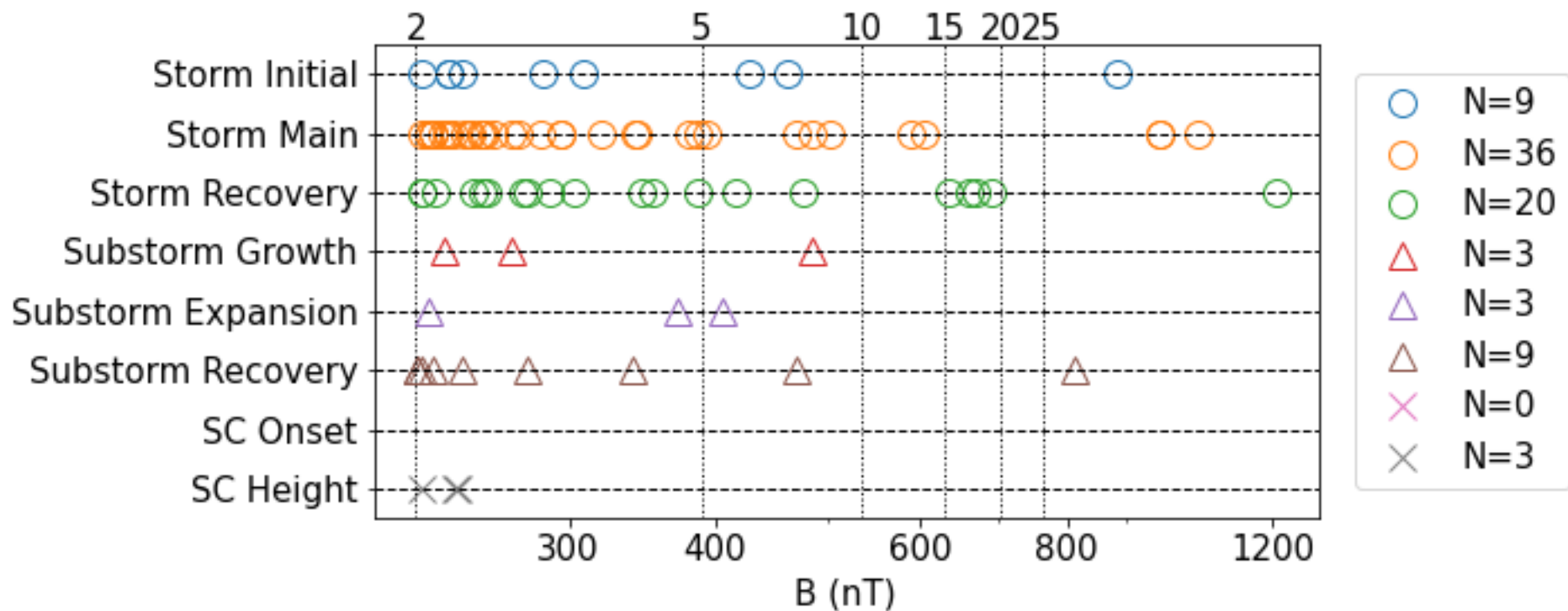


Figure 6.

